

## Prequalification of a set of buckling restrained braces: Part II – numerical simulations

Ciprian Ionut Zub\*<sup>1</sup>, Aurel Stratan<sup>1a</sup> and Dan Dubina<sup>1,2b</sup>

<sup>1</sup>Department of Steel Structures and Structural Mechanics, Politehnica University of Timisoara,  
Ioan Curea, no. 1, 300224, Timisoara, Romania

<sup>2</sup>Fundamental and Advanced Technical Research Centre, Romanian Academy, Timisoara Branch  
Bd. Mihai Viteazu, no. 24, 300223 Timisoara, Romania

(Received September 18, 2019, Revised January 14, 2020, Accepted January 15, 2020)

**Abstract.** Buckling restrained braces (BRBs) were developed as an enhanced alternative to conventional braces by restraining their global buckling, thus allowing development of a stable quasi-symmetric hysteretic response. A wider adoption of buckling restrained braced frames is precluded due to proprietary character of most BRBs and the code requirement for experimental qualification. To overcome these problems, BRBs with capacities corresponding to typical steel multi-storey buildings in Romania were developed and experimentally tested in view of prequalification. In the second part of this paper, a complex nonlinear numerical model for the tested BRBs was developed in the finite element environment Abaqus. The calibration of the numerical model was performed at both component (material models: steel, concrete, unbonding material) and member levels (loading, geometrical imperfections). Geometrically and materially nonlinear analyses including imperfections were performed on buckling restrained braces models under cyclic loading. The calibrated models were further used to perform a parametric study aiming at assessing the influence of the strength of the buckling restraining mechanism, concrete class of the infill material, mechanical properties of steel used for the core, self-weight loading, and frame effect on the cyclic response of buckling restrained braces.

**Keywords:** buckling restrained brace; FEM model calibration; modelling of cyclic response; Abaqus

### 1. Introduction

Buckling restrained braces (BRBs) were developed as an enhanced alternative to conventional braces by restraining their global buckling, thus allowing development of a stable and quasi-symmetric hysteretic response.

The companion paper (Stratan *et al.*, in press) reports experimental tests aiming at seismic prequalification of buckling restrained braces (BRBs) with capacities corresponding to typical steel multi-storey buildings in Romania. Ten full-scale tests on BRBs, as well as uniaxial tests on base materials (steel and concrete) allowed identification of the optimal solution from the point of view of cyclic performance, technology and adjustability.

Though experimental tests are indispensable in development and validation of a new structural component (Park *et al.* 2012, Razavi *et al.* 2018), numerical models are a powerful tool in understanding its response and development of improved solution (Korzekwa and Tremblay 2009). The Finite Element Method (FEM) was used since early 1990's to evaluate the behaviour and to

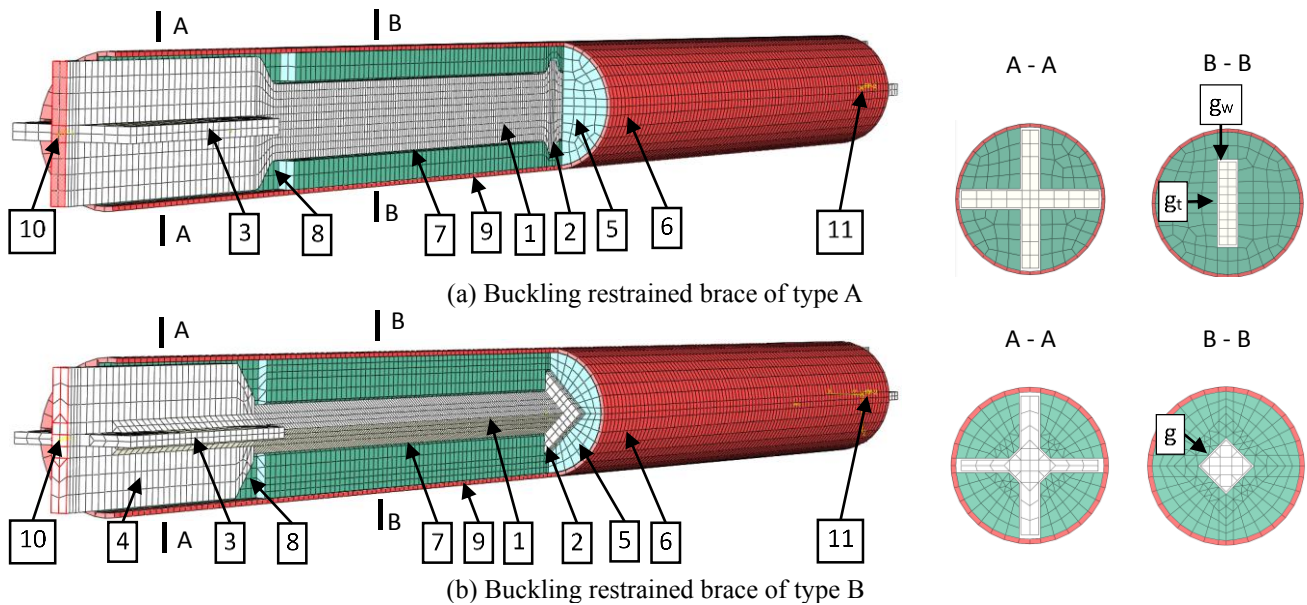
propose design recommendations for BRBs. Inoue *et al.* (1992) used the FEM method to create a two-dimensional model used for determining the size of the reinforced concrete panels depending on the width of the core (steel plate). Saeki *et al.* (1996a) developed and calibrated against experimental results a three-dimensional nonlinear model for BRBs made up of a steel core encased in mortar-filled rectangular steel tube. The FEM model was further used by Saeki *et al.* (1996b) to perform parametric studies for assessing the position of the BRB in a steel frame. Simplified BRB models were used by Matsui *et al.* (2008) to investigate the failure modes of the buckling restraining mechanism (BRM) due to local buckling. Korzekwa and Tremblay (2009) calibrated a FEM model for all-steel BRBs (BRM is a steel assembly) and concluded that the model could be further used for optimizations of BRB components. All-steel dismountable BRBs were numerically investigated by D'Aniello *et al.* (2014). Different solutions for the BRM were also investigated by Rahai *et al.* (2009), Tinker (2011), Rahai and Mortazavi (2014), Yazdi *et al.* (2018). Influence of the plastic to total length ratios of the core on the energy dissipation capacity were investigated using FEM by Pandikkadavath and Sahoo (2016). FEM method was also used to investigate possible failure modes of the BRBs (AlHamaydeh *et al.* 2016), or to evaluate the effect of the loading history and the restraining parameters on the cyclic performance of the BRBs (Ghowsi and Sahoo 2019). During the last decade, new conceptual

\*Corresponding author, Ph.D.

E-mail: [ciprian.zub@student.upt.ro](mailto:ciprian.zub@student.upt.ro)

<sup>a</sup>Associate Professor

<sup>b</sup>Professor



- 1 - Core: mesh size 10 & 20 mm; C3D8I; steel – combined isotropic-kinematic hardening material.  
 2 - Stopper: mesh size 10 mm; C3D8I; steel – combined isotropic-kinematic hardening material.  
 3 - Stiffener: mesh size 20 mm; C3D8I; steel – combined isotropic-kinematic hardening material.  
 4 - Core extension plate: mesh size 20 mm; C3D8I; steel – combined isotropic-kinematic hardening material.  
 5 - Concrete: mesh size 20 mm; C3D8R; concrete – plastic (rectangular core BRBs) / elastic (square core BRBs) material model.  
 6 - Tube: mesh size 20 mm; S4R; steel – kinematic hardening material.  
 7 - Unbonding interface: gap + contact law (normal “Hard”; tangential “Penalty”, 0.1 friction coefficient). Core-to-concrete gap: through thickness/width direction,  $g_t / g_w$ ; uniform gap,  $g$ .  
 8 - Gap for compression stroke,  $L_G = 70$  mm.  
 9 - Contact law: concrete-to-tube composite effect (normal “Hard”; tangential “Penalty”, 0.4 friction coefficient).  
 10 - Fixed support-1: ( $U_x = U_y = U_z = UR_y = UR_z = UR_x =$  constrained).  
 11 - Fixed support-2: ( $U_x = UR_y = UR_z =$  constrained;  $U_z / U_y / UR_x =$  applied longitudinal / transversal / rotational cyclic loading)

Fig. 1 Finite element model

designs of BRBs were developed based on numerical simulations: reduced length BRBs (Razavi *et al.* 2012), ultra-lightweight BRBs (Dusicka and Tinker 2013); inspectable BRBs (Wu *et al.* 2014); self-centering BRBs (Xie *et al.* 2016), and others. As the FEM computer programs evolved in complexity, even coupled nonlinear thermal-stress analyses could be performed on three-dimensional BRB models with either circular (Talebi *et al.* 2014) or rectangular cross-section (Talebi *et al.* 2015). In comparison to the complex three-dimensional models presented above, simplified BRB models consisting of frame elements can be used for fragility assessment of frames equipped with BRBs under different levels of earthquake intensities (Ghowsi and Sahoo 2015).

Based on the above-mentioned studies, it can be concluded that, if using proper modelling hypotheses, the FEM analyses can be used as a reliable method to investigate parameters that could not be evaluated or observed during the experimental tests on BRBs.

Therefore, this paper presents the development of a finite element model of a buckling restrained brace in Abaqus (Dassault 2014) software package and its validation with experimental results. Calibration at both component

and BRB level is presented in detail. The numerical model is used to investigate in detail the tested BRBs, to validate the design methodology of the buckling restraining mechanism, to determine the appropriate class of concrete to be used for the infill material, to determine the influence of the steel grade of the core, and to assess the influence of the frame effect on the BRB cyclic behaviour.

## 2. Calibration of a finite element model of the buckling restrained brace

### 2.1 Model description

Throughout the years, FEM models of different levels of complexity have been proposed for BRBs. Two-dimensional models were used by Eryasar (2009) and Gena and Gelfi (2012), while three-dimensional models were used by Budahazy and Dunai (2015), and AlHamaydeh *et al.* (2016), among others. To reduce computational time, quarter models were preferred by several researchers (Saeki *et al.* 1996a, Mustapha 2013, Montazerian and Mohammadreza 2015). To consider in plane bending of the

core, half-length models were used by Korzekwa and Tremblay (2009). The predictions of full and quarter models under cyclic loading was investigated by AlHamaydeh *et al.* (2016) and close matching was obtained.

Half or quarter models offer the advantage of reduced number of finite elements and, consequently, smaller computational time. However, these models are not appropriate when the response of the BRB is not symmetrical, as might be caused by self-weight loading. Considering that one of the objectives of this study was assessment of the effect of self-weight loading on the response of a BRB, a three-dimensional full model was used.

Finite element models were created for each BRB specimen that was experimentally tested (see Stratan *et al.*, in press). All BRB models have several common features: types of finite elements, type of material models, boundary conditions, geometrical nonlinearities, contact laws. The differences between the models relate to the geometry and material input. Fig. 1 presents a summary of FEM modelling per BRB typology.

A special interest was given to the discretization of the steel core since it is the only component supposed to undergo large plastic deformations under repeated cycles. Different finite elements were used by researchers to discretize the core: shell elements (Matsui *et al.* 2008, Eryasar 2009, Rahai *et al.* 2009), first order brick elements (Chou and Chen 2010, Hoveidae and Rafezy 2012) or second order brick elements (Korzekwa and Tremblay 2009, Razavi *et al.* 2014). In this study the core was modelled using incompatible mode eight-node linear brick elements, C3D8I, which are appropriate to model bending with contact interactions and avoid shear locking or hourglass modes (Dassault, 2014). Two finite elements per thickness were used (as recommended by Korzekwa and Tremblay 2009) and, for the plastic zone, an aspect ratio of approximately 1:1 was considered, thus resulting cubic finite elements (FE). A finer mesh was assigned to the plastic zone (FE size approx. 10 mm), while a coarser mesh for the elastic zones (FE size approx. 20 mm).

Several modelling approaches were used for the buckling restraining mechanism, BRM. A simplified shell or beam model was used by Matsui *et al.* (2008) and Tinker (2011), respectively. Other researchers explicitly modelled the concrete-infill with brick elements and the tube with shell elements (Rahai *et al.* 2009, Guo *et al.* 2017). In this study, the components of the BRM were modelled explicitly and discretized using a coarse mesh. The concrete part was modelled using eight-node linear brick elements with reduced integration and hourglass control, C3D8R, with a global mesh size of 20 mm. The steel tube and the caps were modelled using a four-node doubly curved shell with reduced integration and hourglass control, S4R, due to their reduced thickness, with a global mesh size of 20 mm.

The unbonding material was not modelled explicitly due to its reduced thickness. Instead, a core-to-concrete gap and a contact law were used, as discussed in section 2.4. The polystyrene parts placed at the end of transition zones were modelled using a gap of length  $L_G = 70$  mm.

A general contact was defined. The contact domain consists of two selected surface pairs having different contact properties, as follows. The core-to-concrete interaction was defined as having the tangential behaviour of "penalty" type with the friction coefficient set to 0.1 and the normal behaviour set to "hard" contact. The steel casing-to-concrete interaction had the same properties except the friction coefficient set to 0.4. In both cases, the metallic surfaces were considered "master" in the contact formulation to avoid excessive penetrations and numerical errors. Also, a coupling constraint was defined at each end of the core, by connecting a reference point to the end surface of the core using kinematic coupling.

## 2.2 Boundary conditions and loading

To the authors' knowledge, there are no numerical studies on BRBs that considers both the cyclic and the self-weight loadings. Furthermore, if rigid (bolted or welded) BRB-to-gusset connections are used to insert the BRB in the (testing) frame, additional bending moments are transmitted to the BRB ends due to the frame effect (opening and closing of the beam-to-column angle). These additional moments were modelled by Saeki *et al.* (1996b) using an "obliquely loaded model", while Dusicka and Tinker (2013) used load eccentricity applied at each BRB end. As regarding the applied cyclic loading, most researchers used the displacement control applied to either one end (Dusicka and Tinker 2013) or to the both ends of the BRB (Chen *et al.* 2016).

In this study the definition of the boundary conditions consisted in assigning fixed supports at the BRB ends (at the reference points) and applying the self-weight and the cyclic load to assure similar conditions as in the experimental tests. The supports have the translational ( $U_i$ ) and rotational ( $UR_i$ ) degrees of freedom constrained with respect to axis  $i$ .

The self-weight load was applied taking into account the position of the specimen in the experimental setup. Special consideration was given to modelling the cyclic load due to the fact that the BRBs were experimentally tested using the BRB-column sub-assembly setup. This setup causes frame effects due to opening and closing of the angle  $\theta$ , Fig. 2(a), during the tension/compression phases. In the finite element model of the testing sub-assembly, the column and the gusset-plate connections were not modelled, only the BRB in between the gussets. To simulate the frame effect due to rigid body rotation of the column, Fig. 2(a), transversal displacement  $U_y$  and rotations  $UR_x$  were applied at one of the BRB ends, in addition to the axial displacement  $U_z$ , Fig. 2(b). The axial displacement  $U_z$ , the transversal displacement  $U_y$  and rotation  $UR_x$  were determined by imposing the lateral drift of the test assembly  $\Delta_b$  and considering rigid body rotation of the column-gusset assembly (Fig. 2(b)).

As presented in the companion paper (Stratan *et al.* in press), the loading protocol used for experimental tests was based on ANSI/AISC 341-10 (2010) provisions, but with additional cycles. The loading sequence consisted of 2

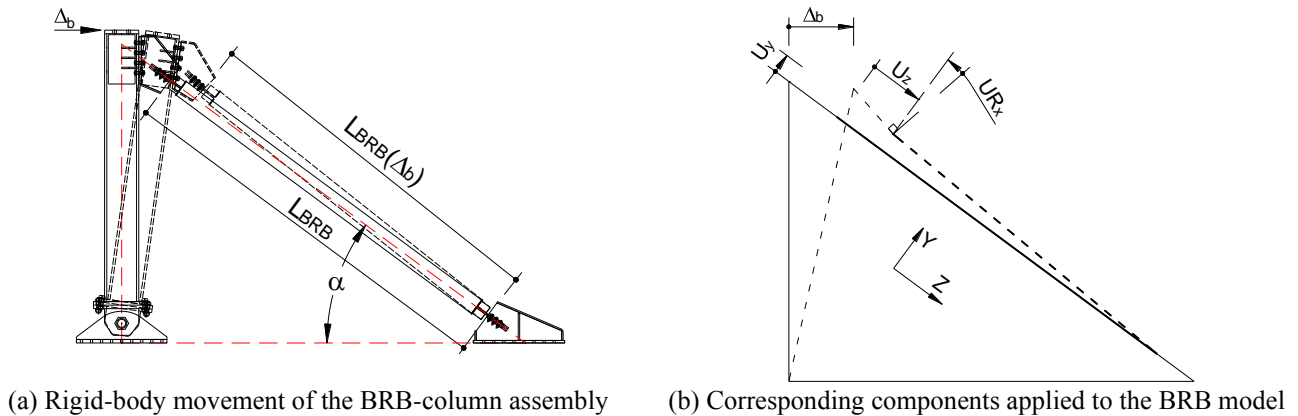


Fig. 2 Modelling of cyclic loading

cycles at each of the following amplitudes:  $\Delta_{by}$  (depending on the specimen),  $0.5\Delta_{bm}$  (25.6 mm),  $1.0\Delta_{bm}$  (51.2 mm),  $1.5\Delta_{bm}$  (76.8 mm),  $2.0\Delta_{bm}$  (102.4 mm),  $2.5\Delta_{bm}$  (127.9 mm, additional cycles), followed by cycles at  $1.5\Delta_{bm}$  until failure was attained ( $\Delta_{by}$  is the yield deformation of the BRB,  $\Delta_{bm}$  is the design inter-storey drift). The same loading protocol was used for calibration of BRB models.

### 2.3 Analysis and validation

Different Abaqus procedures can be used to solve the nonlinear equations. Static procedures incorporating also numerical techniques to improve the convergence rate were used by Hoveidae and Rafezy (2012), Dehghani and Tremblay (2017), Yazdi *et al.* (2018). Explicit formulation was used by Hadianfard *et al.* (2018).

Due to the high nonlinearity of the full three-dimensional model, the FEM analyses were performed using the Dynamic Explicit solver. Three steps were defined: initial, self-weight, cyclic. In the initial step, the model and the initial geometrical imperfection (see section 2.6) are defined. In the second step, the self-weight load is applied using a smooth step amplitude to avoid dynamic effects. In the third step, with the self-weight load kept constant, the cyclic load is applied using a smooth step amplitude function to assure a quasi-static analysis. For the last two steps, nonlinear effects considering large deformations and displacements were considered.

Assessment of output energy balance must be performed to assure reliable FEM results (Korzekwa and Tremblay 2009). The energy balance was monitored to check the analysis: kinetic energy was under 1% of the internal one, thus assuring a quasi-static analysis; artificial energy was also low, under 1% of the internal energy, thus validating the finite elements used (no shear locking of hourglass deformation modes of the elements). External work and internal energy had an almost similar path throughout the analysis, thus validating the results obtained.

### 2.4 Unbonding material

Due to the fact that the unbonding material has a relatively small thickness compared to the thickness of the

core, in most cases it is not modelled explicitly. Instead, a gap and a contact law are used (Rahai *et al.* 2009, AlHamaydeh *et al.* 2016, Budahazy and Dunai 2015). However, Eryasar (2009) used planar shell elements with elastic mechanical properties to explicitly model the unbonding material. In this study the first approach was used.

The acrylic tape was modelled by using a gap and a contact law. The size of the gap was set equal to the nominal thickness of the unbonding layer, which are described in Stratan *et al.* (in press). The definition of the contact law includes a normal “Hard” and a tangential “Penalty” behaviour. For the tangential behaviour different values of the friction coefficient (0.05, 0.1, 0.2, 0.3) were numerically tested on the BRB model corresponding to CS33-1. The BRB specimen CS33 was chosen for this calibration since the material used to model the core was calibrated based on uniaxial cyclic test data and does not represent an unknown variable. Good agreement with the experimental results (CS33-1) was obtained by using a friction coefficient equal to 0.1, see Fig. 3 (Guo *et al.* 2017). Also, the higher the friction (0.2 or 0.3), the higher is the compression overstrength and less ductile is the BRB. Using less friction (0.05) leads to lower compression overstrength and no fracture occurs, contrary to the experimental results.

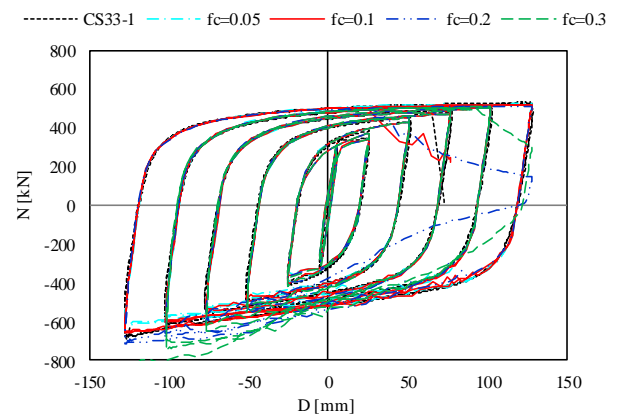


Fig. 3 Calibration of the value of the friction coefficient

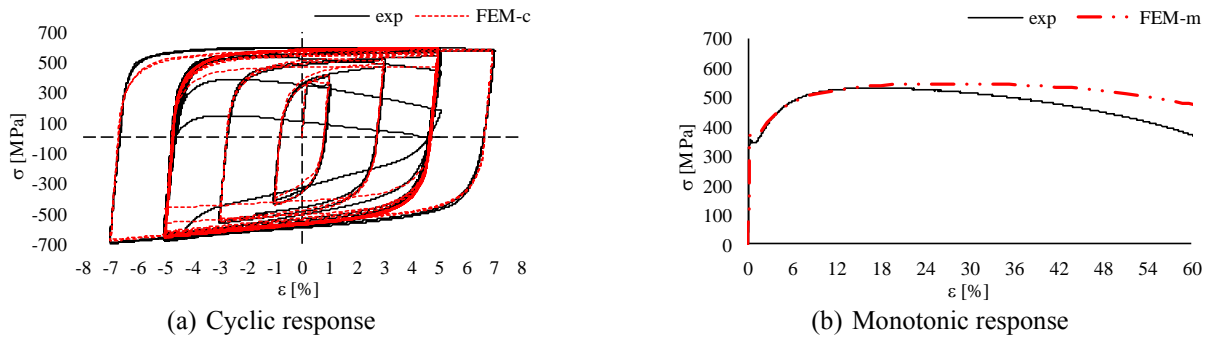


Fig. 4 Calibrated FEM response of core material C30 for the specimens CS33-1 and CR33-2

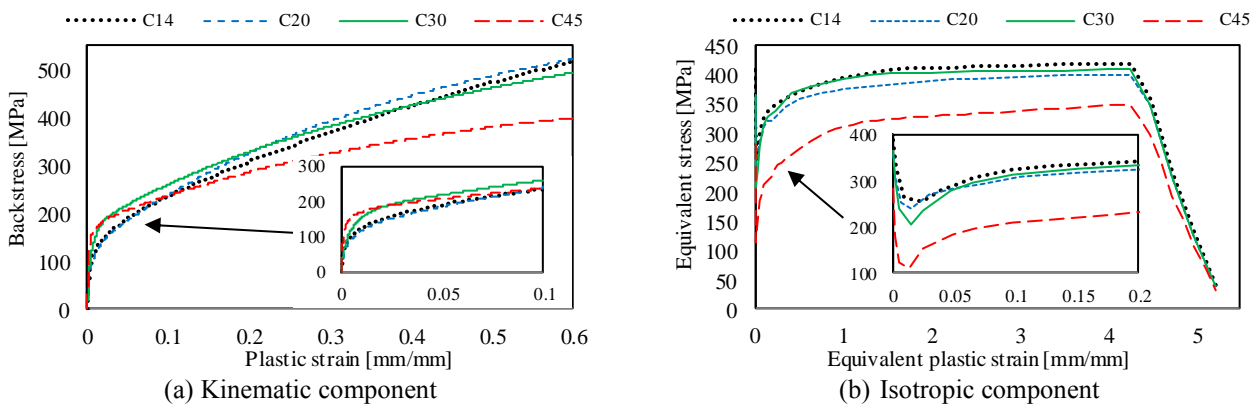


Fig. 5 Calibrated inputs of core materials

## 2.5 Material models

### 2.5.1 Steel

Built-in material models are generally used to model both the elastic and plastic behaviour of BRB steel components. The combined isotropic-kinematic hardening model is used by most researchers to model the steel core as it allows good representation of the Bauschinger and cyclic hardening phenomena (Korzekwa and Tremblay 2009, Chen *et al.* 2016). However, for closer predictions user material subroutines were developed and implemented in Abaqus and Ansys finite element computer programs by Piedrafita *et al.* (2015) and Budahazy and Dunai (2015), respectively. In this study Abaqus built-in models were used.

Two different material models were used for steel parts of BRBs: kinematic and combined. Both models have the same definition of the elastic component (steel elastic modulus,  $E_s = 210000 \text{ N/mm}^2$  and Poisson's ratio  $\nu = 0.3$ ), but different definitions of the plastic component.

In the case of steel tubes, the plastic hardening behaviour was defined using the kinematic option, since the tubes are not expected to experience cyclic plastic deformations. Thus, a simple bilinear model (elastic-plastic with strain hardening) was appropriate for FEM modelling of the tubes. Based on the data from the quality certificates, the kinematic material inputs expressed as true yield stress,

Table 1 Material inputs for steel tubes

CHS 168.3x4		CHS 177.8x4		CHS 193.7x6.3	
$\sigma^0$	$\varepsilon^{pl}$	$\sigma^0$	$\varepsilon^{pl}$	$\sigma^0$	$\varepsilon^{pl}$
N/mm <sup>2</sup>	mm/mm	N/mm <sup>2</sup>	mm/mm	N/mm <sup>2</sup>	mm/mm
345.6	0.000	460.0	0.000	338.5	0.000
489.9	0.147	645.2	0.129	432.6	0.152

$\sigma^0$ , and true plastic strain,  $\varepsilon^{pl}$ , were obtained, and are presented in Table 1.

A more complex material model, with combined isotropic-kinematic hardening, was used to model the steel core. The model consists of a nonlinear kinematic component and a multilinear isotropic (cyclic) hardening component. Based on the von Mises yield criterion and Chaboche (Lemaitre and Chaboche 1990) plastic hardening model, the combined model can simulate the Bauschinger effect due to cyclic loading (Dassault 2014). The multilinear definition of the cyclic hardening allows for the simulation of the yield plateau and the increase (or decrease) of the yield surface under repeated cycles at constant strain. Further details regarding the calibration of the input parameters of the core material are available in (Zub *et al.* 2018).

Table 2 Calibrated parameters describing the kinematic hardening of the core material models

Material	$\sigma^0$ N/mm <sup>2</sup>	$C_1$ N/mm <sup>2</sup>	$\gamma_1$ -	$C_2$ N/mm <sup>2</sup>	$\gamma_2$ -	$C_3$ N/mm <sup>2</sup>	$\gamma_3$ -	$C_4$ N/mm <sup>2</sup>	$\gamma_4$ -	$C_5$ N/mm <sup>2</sup>	$\gamma_5$ -
C14	407.77	45000	850	12600	245	1900	35	630	1.3	210	1
C20	359.46	40000	900	10000	195	2000	67	950	3.5	350	1
C30	367.08	41513	697	15152	137.5	600	4.6	255	2.2	195	0
C45	282.13	95000	1300	40500	680	5000	120	500	2.5	200	2

Table 3 Calibrated parameters describing the isotropic hardening of the core material models

	$\sigma^0$ , N/mm <sup>2</sup>	$\varepsilon^{pl}$ , -	$C_1$	$\gamma_1$	$C_2$	$\gamma_2$	$C_3$	$\gamma_3$	$C_4$	$\gamma_4$	$C_5$	$\gamma_5$
C14	407.8	0.0	256.7	0.0237	289.6	0.0488	324.6	0.0962	340.0	0.166	350.0	370.0
											395.3	412.3
											419.5	356.6
											4256	4.476
											5.226	
C20	359.5	0.0	239.2	0.0149	284.0	0.0488	312.0	0.1035	320.0	0.150	333.0	358.0
											376.0	390.0
											401.0	349.4
											4.256	4.476
											5.226	
C30	367.1	0.0	206.1	0.0139	278.4	0.0464	313.5	0.0966	326.8	0.150	339.1	368.9
											393.4	404.6
											410.2	348.7
											4.256	4.476
											5.226	
C45	282.1	0.0	112.0	0.0134	185.0	0.0488	211.7	0.0974	220.5	0.140	245.0	274.0
											311.0	329.5
											349.8	297.3
											4.256	4.476
											5.226	

The combined model is loading-history dependent from the point of view of isotropic hardening definition (Zub *et al.* 2018). Therefore, calibration of the isotropic model must be performed using experimental results from a uniaxial coupon test having a loading history similar to the one used for testing the BRBs, with respect to the strain evolution recorded during BRB cyclic testing. Based on these observations, the calibration of the core material C30 used for BRB FEM model CS33 was focused on predicting the cyclic behaviour under variable amplitude loading. The capability of the combined model to reproduce with a certain level of accuracy both the cyclic and monotonic behaviour of mild carbon steel with respect to experimental data is presented in Figs. 4(a) and 4(b).

For the other BRB cores, where no cyclic material test data were available, the calibration of the material model was performed using a trial-and-error procedure using the force ( $N$ ) – displacement ( $D$ ) cyclic curve of the BRBs. Having as fixed parameter the yield stress and zero plastic strain,  $\sigma^0$ , the trial and error procedure was focused on determining the appropriate values of the kinematic hardening moduli,  $C_k$ , and their corresponding decreasing rate,  $\gamma_k$ , with respect to increasing plastic deformation.

In Fig. 5 calibrated core material inputs are graphically presented for both kinematic, see Fig. 5(a), and isotropic component, see Fig. 5(b). The calibrated kinematic and isotropic hardening parameters are presented in a tabular form in Tables 2 and 3, respectively.

### 2.5.2 Concrete

The concrete material model proved to have an important role when calibrating the specimens CR71-1 and CR71-2 that buckled during tests. Therefore, the performance of two approaches for modelling the concrete

infill were assessed on the FEM model of the CR71-1 specimen.

For modelling infill concrete, test results on cubes cured in room conditions were used. The mean value of compressive cube strength of concrete is  $f_{c,cube} = 47.3$  N/mm<sup>2</sup> (Stratan *et al.* in press). Using the provisions from EN 1992-1-1 (2004) the other mechanical properties were determined and are summarized in Table 4. The mean value of the compressive cylinder strength of concrete was obtained as  $f_{cm} = 0.8f_{c,cube}$ . The linear elastic compressive limit was set to  $0.4f_{cm}$ . The mean value of axial tensile strength of concrete,  $f_{ctm}$ , was computed based on the characteristic compressive cylinder strength of concrete,  $f_{ck}$ , using the equivalent formula,  $f_{ctm} = 0.3f_{ck}^{2/3}$ , where  $f_{ck} = f_{cm} - 8$  N/mm<sup>2</sup>. The value of the secant modulus of elasticity of concrete was determined as  $E_{cm} = 22[(f_{cm})/10]^{0.3}$ , with  $f_{cm}$  in N/mm<sup>2</sup>. The value of the compressive strain in concrete at the peak stress  $f_{cm}$  was computed as  $\varepsilon_{c1} = 0.7f_{cm}^{0.31} \leq 2.8^{0/00}$ .

The plasticity number was determined as  $k = 1.05E_{cm}|\varepsilon_{c1}|/f_{cm} = 1.96$ .

The first approach consists in modelling the concrete parts using an elastic material (Chou and Chen 2010, Guo *et al.* 2017), see Fig. 6 Secant modulus of elasticity of concrete,  $E_{cm} = 32795$  N/mm<sup>2</sup>, and Poisson's ratio,  $\nu = 0.2$ , define the isotropic elasticity.

Table 4 Mechanical properties of concrete infill

$f_{c,cube}$ N/mm <sup>2</sup>	$f_{cm}$ N/mm <sup>2</sup>	$0.4f_{cm}$ N/mm <sup>2</sup>	$f_{ck}$ N/mm <sup>2</sup>	$f_{ctm}$ N/mm <sup>2</sup>	$E_{cm}$ N/mm <sup>2</sup>	$\varepsilon_{c1}$ -
47.3	37.8	15.2	29.8	2.9	32795	0.00216

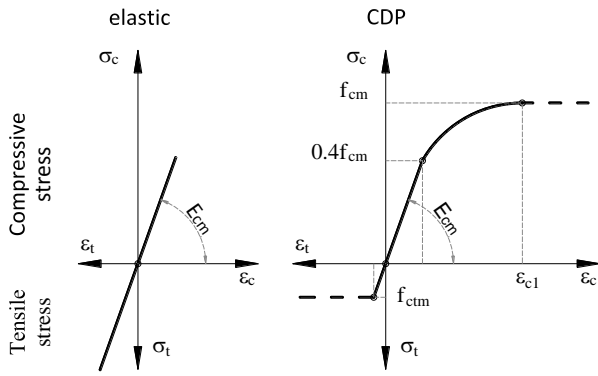


Fig. 6 Stress-strain relationships of concrete

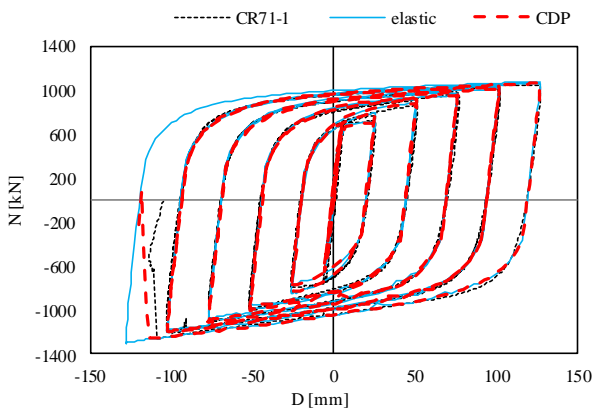


Fig. 7 BRB cyclic predictions using different concrete material models

The second modelling approach uses the Abaqus "built-in" Concrete Damaged Plasticity model, CDP (AlHamaydeh *et al.* 2016, Rahai and Mortazavi 2014). The following parameters define the concrete plasticity (Dassault 2014): dilation angle,  $\Psi = 36^\circ$ ; eccentricity,  $\epsilon = 0.1$ ; ratio of initial equibiaxial compressive yield stress to initial uniaxial compressive yield stress,  $\sigma_{b0}/\sigma_{c0} = 1.16$ ; ratio of the second stress invariant on the tensile meridian to that on the compressive meridian,  $K_c = 0.667$ ; viscosity parameter,  $\mu = 0$ . The constitutive stress-strain curves used to describe the compressive and tensile behaviour of the CDP model are based on a simplified version of the EN 1992-1-1 (2004) definition of the nonlinear behaviour of the concrete material. As graphically presented in Fig. 6, the compressive behaviour has the elastic limit set to  $0.4f_{cm}$ , while the plastic stress-strain relationship is parabolic up to the peak stress  $f_{cm}$  and constant afterwards. The tensile behaviour is defined as elastic-perfectly plastic, with the elastic limit set to  $f_{ctm}$ .

Abaqus requires true stress-strain relationship to define the plastic behaviour of a material model. Therefore, yield stress and inelastic/cracking strain data pairs must be provided for compressive/tensile behaviour (Dassault 2014). To obtain the material input, the nominal stress-strain data pairs (resulted following the provisions from EN

1992-1-1 2004) were transformed into true stress and logarithmic strain using the following formulas:  $\sigma = \sigma_{nom}(1 + \epsilon_{nom})$ ,  $\epsilon = \ln(1 + \epsilon_{nom})$ . After deducting the elastic part, the compressive behaviour is expressed as yield stress and inelastic strain data pairs  $(\sigma^i; \epsilon^{in})$ , with the first pair ( $i = 1$ ) defined as  $(\sigma^1; 0.0)$ , where  $\sigma^1 \approx 0.4f_{cm}(1 + 0.4f_{cm}/E_{cm})$  is the initial compressive yield stress. The tensile behaviour is defined by only one yield stress and cracking strain data pair  $(\sigma^1; 0.0)$ , with  $\sigma^1 = f_{ctm}(1 + f_{ctm}/E_{cm})$ .

As it can be observed in Fig. 7 the elastic concrete model overpredicts the cyclic response of the specimen CR71-1 at large core deformations, since no plastic deformations take place in the concrete part and, therefore, the material fully recovers when unloading. Instead, the CDP model leads to close prediction with the experimental response of specimen CR71-1 at global buckling, since irreversible plastic deformation can take place in the concrete part, reducing the stiffness. Nevertheless, an elastic concrete model is a reasonable simplification if the BRM is not susceptible to global buckling.

Based on the above observations, the CDP model was considered appropriate to model CR71 specimens (CR71-1, CR71-2) since they experimentally buckled and, which led to plastic deformations in the concrete parts of the FEM model. The same concrete model was used in the case of the other BRB models of type A (CR33-1 /-2 and CR73-1 /-2) due to consistency reasons (the case of the CR33 model) and due to the fact that the influence of concrete class is numerically investigated on the CR73 model. As regarding the other BRBs that did not fail by global buckling, the response of the concrete parts is expected to be mostly elastic. Therefore, an elastic concrete model was used for finite element models of BRBs of type B (CS33-1 /-2, CS73-1 /-2), which proved to be efficient in reducing the numerical errors caused by excessive penetrations of the core into the concrete parts in the elastic zone.

### 2.6 Geometrical imperfections

The initial geometrical imperfections of BRBs can be classified as those due to the deviation from the rectilinear shape of the steel core (misalignment of the core components, core off-centring relative to steel tube) and those of the steel tube (bow imperfections and misalignment of connections). Core imperfections were not determined due to the difficulties in assuring reliable measurements: the core is very slender and has large initial deflections; after concrete casting, the position of the core relative to the tube cannot be determined precisely. Instead, tube imperfections were measured and a bow shape imperfection was obtained with a maximum amplitude of  $e_{0,max} = L_{BRB}/14036 = 0.28$  mm, with respect to BRB length ( $L_{BRB}$ ).

According to EN 1993-1-1 (2005), equivalent geometric imperfections must be used in structural analyses with values that reflect the possible effects of all types of imperfections (geometrical misalignments, loading eccentricities). Consequently, an initial equivalent geometrical bow imperfection ( $e_0$ ) was introduced in the BRB FEM model by using the first buckling mode, whose

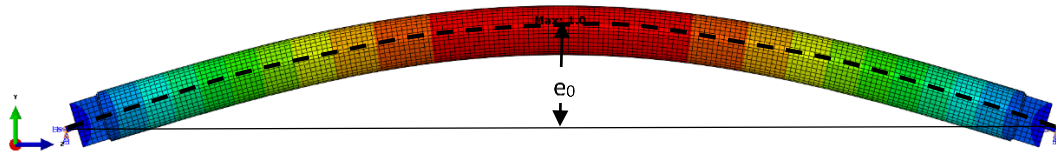


Fig. 8 Equivalent geometric bow imperfection

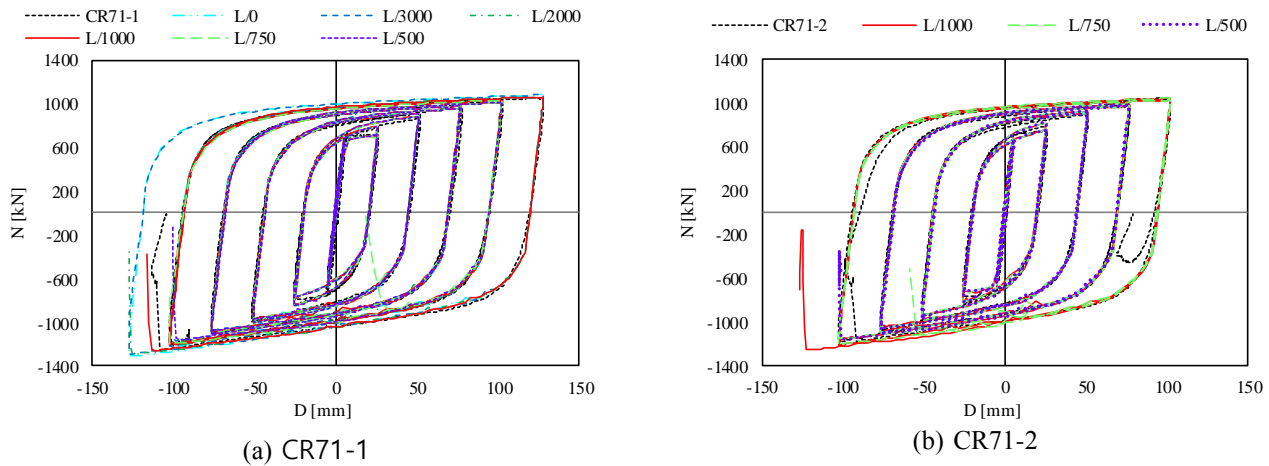


Fig. 9 Effect of initial geometrical imperfections on BRB FEM models CR71

deformed shape was in the YZ plane of the self-weight load (Fig. 8).

Since it was not possible to measure all possible geometrical imperfections, an equivalent bow imperfection  $e_0$  was determined by performing cyclic FEM analyses on CR71 models and comparing the predictions with the experimental results. Different values for  $e_0$  ( $0$ ,  $L_{BRB}/3000$ ,  $L_{BRB}/2000$ ,  $L_{BRB}/1000$ ,  $L_{BRB}/750$ ,  $L_{BRB}/500$ ) were considered. As it can be observed in Fig. 9(a), in the case of BRB model CR71-1 close predictions are obtained using an initial bow imperfection of  $L_{BRB}/1000$ . In the case of BRB model CR71-2, see Fig. 9(b), an imperfection of  $L_{BRB}/750$  leads to closer agreements with the experimental results. As an imperfection of  $L_{BRB}/750$  caused premature buckling in the case of BRB model CR71-1, an initial equivalent bow imperfection of  $e_0 = L_{BRB}/1000$  (Hoveidae and Rafezy 2012, Guo *et al.* 2017) was applied for all other BRB models.

### 2.7 Model calibration

Using the above-mentioned FEM modelling hypotheses (material models, initial imperfections, contact laws), geometrically and materially nonlinear analyses including imperfections (GMNIA) were performed on FEM models of BRBs under cyclic loading. The predictions in terms of reaction force ( $N$ ) and end displacement ( $D$ ) are presented in Fig. 10 in comparison with experimental results. As a general remark, the BRB FEM models reproduce the experimental hysteresis loops with a good level of accuracy. The failure of the core in tension due to excessive necking is captured for all models. Except for the models that failed by global buckling (CR71-1 and CR73-2), in the case of all

the other BRB models the failure mode is by fracture of the core in the plastic zone during tensile loading. It is to be mentioned that the failure of the material due to low-cycle fatigue was not explicitly included in the material model.

For the CR71 specimens (CR71-1, CR71-2), the model predictions are quite accurate. The FEM model was able to capture both the cyclic behaviour and the failure mode by global buckling of the BRBs.

In the case of CR73 specimens, the predicted cyclic response has an acceptable level of accuracy, since between the two experimental responses (CR73-1 and CR73-2) there were minor differences. For the first model, CR73-1, the failure occurred prematurely during the tensile phase of the 11<sup>th</sup> additional cycle at  $1.5\Delta_{bm}$ . Thus, the model was able to perform only 23.25 out of 25.0 cycles, as experimentally recorded. In the case of FEM model CR73-2, the failure occurred also prematurely during the tensile phase of the 9<sup>th</sup> additional cycle at  $1.5\Delta_{bm}$ . Thus, the model was able to perform only 21.5 out of 25.5 cycles, as experimentally recorded. In both cases, the FEM models developed larger compression hardening during the additional cycles at  $1.5\Delta_{bm}$  due to material input.

Close predictions were also obtained for both CR33 specimens (CR33-1, CR33-2). The FEM models were not able to fully capture the excessive hardening during compression cycles corresponding to  $2.5D_{bm}$ . This might be caused by the material input used for the core, for which no experimental data was available for calibration.

From FEM results it was observed that the excessive hardening response at large deformations in compression is caused by increasing of the cross-sectional area of the core as a result of the Poisson's effect. The increase took place

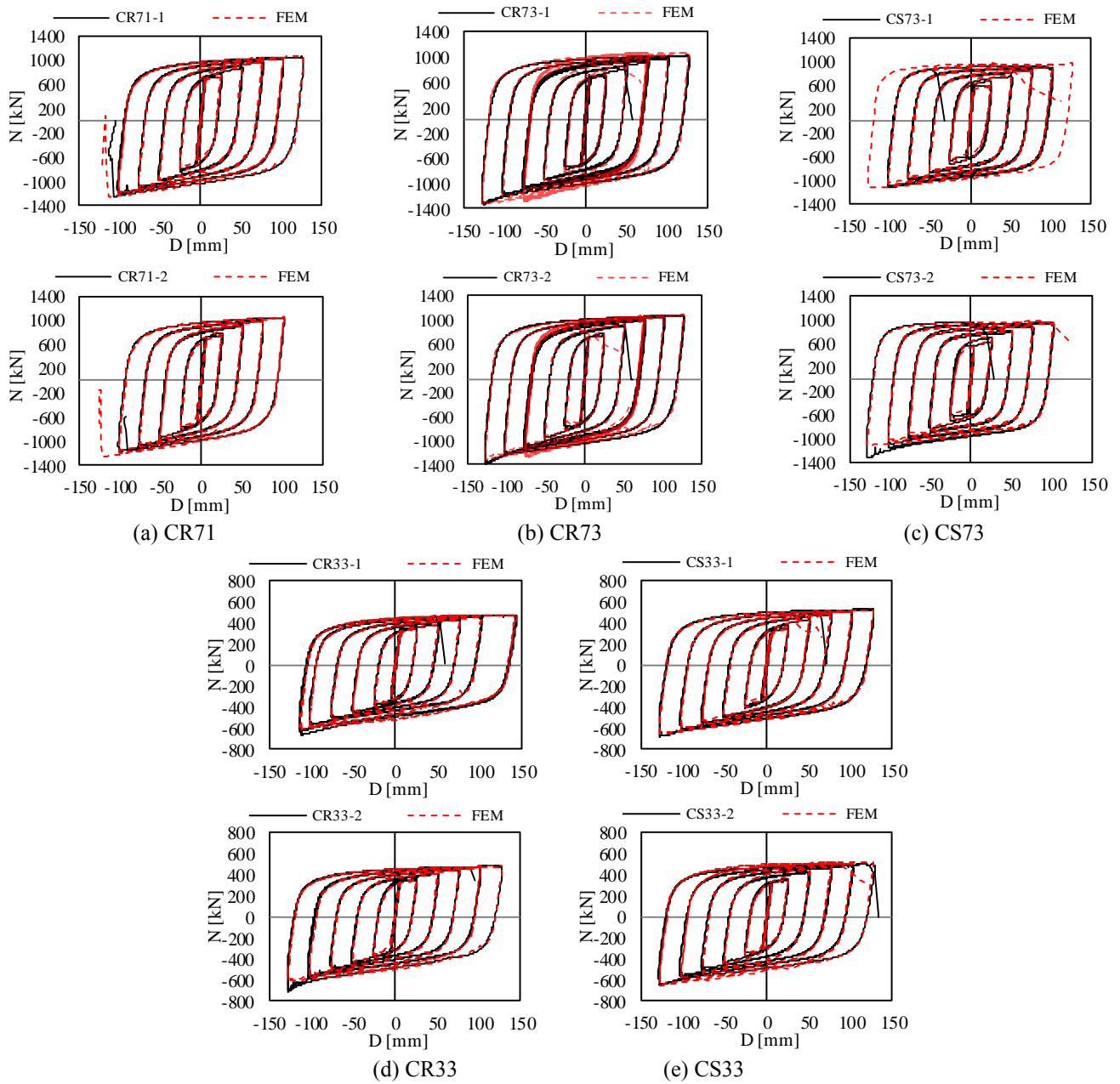
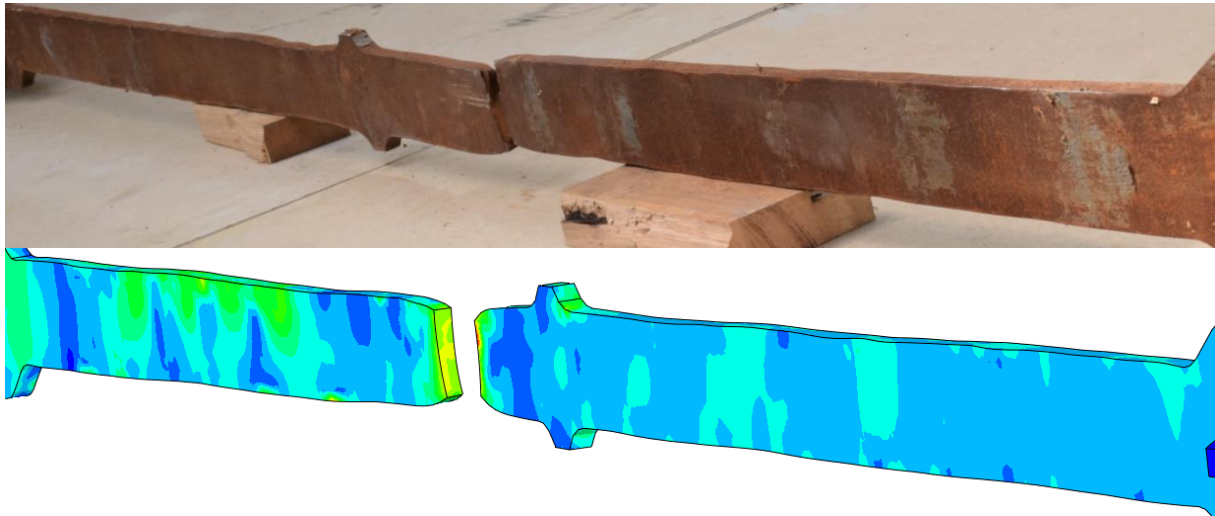


Fig. 1 Calibration of FEM BRB models based on experimental results

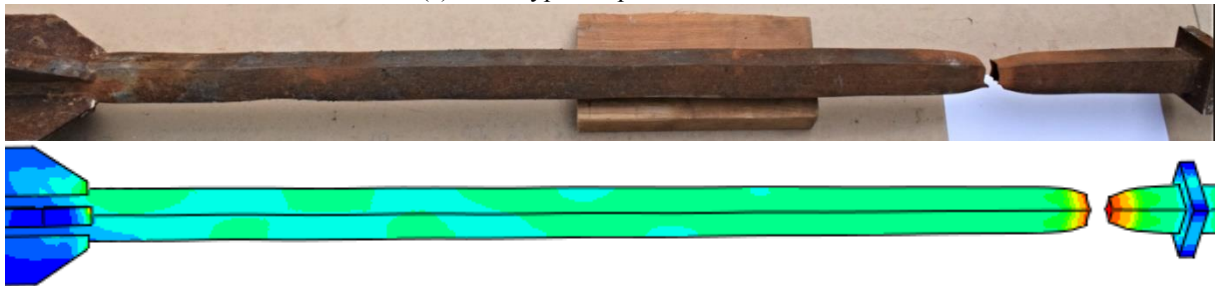
mainly in the through-width direction of the plastic segment of the core, which is located near the transition zones. Therefore, the stress flow finds a new path, through the concrete part, leading to higher compression forces and un-symmetric cyclic response. Further investigations are required to properly determine the thickness of the unbonding material with respect to the Poisson's effect under large strains.

In the case of CS33 specimens, since cyclic material test data were available for calibration, the BRB models were able to predict with a very good level of accuracy both the cyclic response and the failure mode. As in the case of CR73 specimens, there are minor differences between the response of two experimental specimens (CS33-1, CS33-2).

Regarding CS73 specimens, there are some differences between the experimentally obtained hysteresis loops due to the manufacturing imperfections (misalignment of the core components). When comparing the experimental and FEM results, it can be noticed that the cyclic performance of the specimen CS73-1 was considerably reduced due to misalignments of the components. The FEM model CS73-1 was able to sustain an extra complete cycle at  $2.5\Delta_{bm}$  prior fracture in tension. In the case of CS73-2 specimen, excessive hardening response at the first compression cycle corresponding to  $2.5\Delta_{bm}$  was recorded. The FEM BRB model is not able to capture this phenomenon and therefore is considered to be caused by manufacturing imperfections

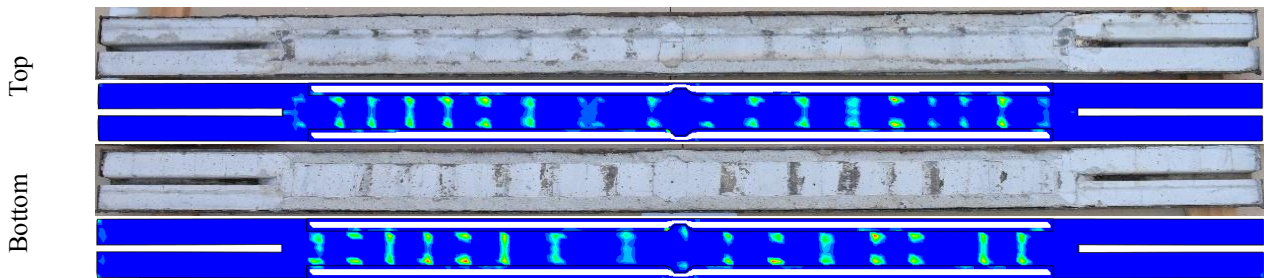


(a) BRB Type A: specimen CR73-2

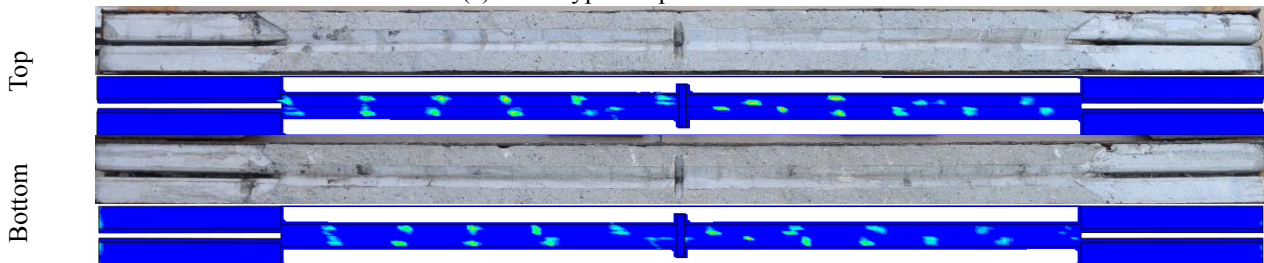


(b) BRB Type B: specimen CS73-2

Fig. 2 Deformed shape of BRB core: experimental vs. FEM



(a) BRB Type A: specimen CR73-2



(b) BRB Type B: specimen CS73-2

Fig. 3 Friction zones on concrete infill: experimental vs. FEM

(misalignment of polystyrene parts). Also, close prediction of the fracture was obtained for CS73-2 specimen. Based on the above observations, the numerical BRB models were

able to capture the cyclic behaviour of the specimens CS73-1 and CS73-2 with an acceptable level of accuracy.

In Figs. 11(a) and 11(b) are presented both the experimental and FEM deformed shape of the cores for two BRBs, CR73-2 and CS73-2. It can be observed that fracture positions are relatively close to the stopper, as in the experimental cases. Also, the core of CR73-2 model is more deformed about the minor axis of inertia, while the core of CS73-2 is more uniformly deformed with respect to the principal axes of inertia.

In Figs. 12(a) and 12(b) are presented the friction zones on the concrete infill in FEM model in comparison to the experimental specimens, CR73-2 and CS73-2. A larger number of friction zones can be observed in the case of the CR73-2 model since the cross-section is rectangular and has a small axis of inertia, while in the case of CS73-2 model the core has a compact square cross-section shape.

### 3. Parameters influencing BRB performance

The numerical study aims at understanding some phenomena related to BRB cyclic behaviour and at extending the experimental database by performing parametric FEM analyses on the calibrated BRBs models. Therefore, the influence of the following parameters was numerically investigated: the strength of the buckling restraining mechanism, the class of the concrete infill, the steel grade of the core material, the effect of the self-weight loading.

The cyclic analyses were performed using the loading protocol presented in Fig. 13. It is limited to the first 10 cycles as required by ANSI/AISC 341-10 (2010), since the cumulative inelastic deformation,  $CID$ , for this loading history exceeds the minimum requirement of 200 times the yield deformation of the BRB,  $\Delta_{by}$ .

#### 3.1 BRM strength

Early studies on bucking-restrained braces suggested that global buckling of the BRB can be prevented if the elastic critical force  $N_{cr}$  of the buckling-restraining mechanism (BRM) is at least 1.5 times the nominal resistance of the core  $N_p$  (Watanabe *et al.* 1988). However, some studies (Iwata and Murai 2006) suggested that  $N_{cr}/N_p \geq 3$  is necessary to obtain cumulative inelastic deformations in excess of 200 times the yield deformation, as required by ANSI/AISC 341-10 (2010).

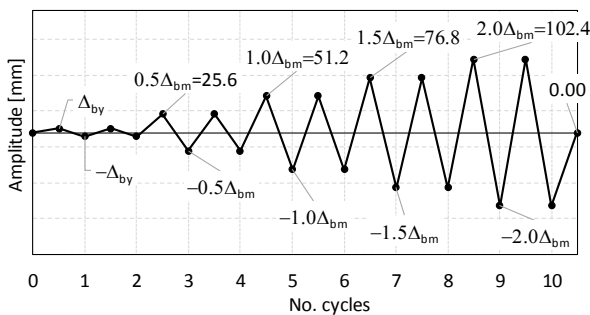


Fig. 13 Loading protocol used for parametric FEM analyses

Takeuchi and Wada (2017) proposed the following expression for design of the buckling restraining mechanism

$$\frac{N_{cr}}{C_{max}} > 1 + \left( \frac{\pi^2 E_s}{2f_y} \cdot \frac{e_0}{L_{BRB}} \right) / \left( \frac{L_{BRB}}{D_e} \right) \quad (1)$$

where:  $C_{max}$  is the maximum compression force developed by the BRB;  $f_y$  is the yield strength of the steel tube;  $e_0$  is the amplitude of the initial bow imperfection, taking into account geometrical imperfections of core, the brace, and of the connections (load eccentricity);  $D_e$  is the exterior diameter of the steel tube.

The initial bow imperfection used in Eq. (1) is difficult to be established. Moreover, Eq. (1) addresses monotonic compression case since there are no factors to take into account the strength degradation of BRM due to cyclic loading.

The influence of the strength of the buckling restraining mechanism (BRM) on the BRB performance was evaluated by assessing the response of five finite element models under monotonic and cyclic loading conditions. The numerical models are based on the calibrated model CR71-1. For each BRB model, the buckling restraining mechanism was designed for different ratios between the elastic critical load of the steel tube,  $N_{cr}$ , and the plastic resistance of the core,  $N_p$ . The following ratios were considered:  $N_{cr}/N_p = 1.50, 1.75, 2.0, 2.5, 2.79$ . The thickness of the steel tube,  $t$ , was offset to the exterior, thus the concrete section did not change from one model to the other.

The critical buckling load was computed based on Euler's formula

$$N_{cr} = \pi^2 E_s I_s / L_{cr}^2 \quad (2)$$

where:  $E_s$  and  $I_s$  are the elastic modulus and the moment of inertia of the steel tube, respectively;  $L_{cr} = L_{BRB} = 3930$  mm is the buckling length of the BRM, considered for this study equal to the length of the BRB.

To check the design Eq. (1), monotonic compression analyses were performed on the BRB models. FEM models of specimens CR71-1 and CR71-2 with different values of the initial geometrical imperfection ( $L_{BRB}/1000, L_{BRB}/500, L_{BRB}/450, L_{BRB}/250$ ) were analysed. The value of the initial imperfection that resulted in best match with the experimental buckling load under cyclic loading was  $e_0/L_{BRB} = 1/450$  (Fig. 14).

Using the calibrated equivalent imperfection for monotonic loading ( $e_0 = L_{BRB}/450$ ), monotonic compression analyses were performed on the other BRB models with varying ratios of  $N_{cr}/N_p$ . The maximum compression force developed by the brace prior to buckling represents the design axial resistance ( $N_{Rd,f}$ ) of the BRM obtained using the FEM method.

Following the analytical approach from Takeuchi and Wada (2017), the design resistance  $N_{Rd,a}$  of the BRM can be obtained with Eq. (3), which is the ratio between the critical elastic force  $N_{cr}$  and the safety factor  $\alpha$  defined by Eq. (4)

$$N_{Rd,a} = N_{cr} / \alpha \quad (3)$$

Table 5 Performance evaluation of BRB models with different  $N_{cr,s}/N_{p,m}$  ratios

$D_e \times t$ mm	$N_{cr}$ kN	$N_{cr}/N_p$ -	$\alpha$ -	$N_{Rd,a}$ kN	$N_{Rd,f}$ (mon.) kN	$C_{max}$ (cyclic) kN	$N_{Rd,f}/N_{Rd,a}$ -	$U_{y,mid}$ mm	$N_{Ed,BRM}/N_{Rd,a}$ -	$N_{Ed,BRM}/N_{Rd,f}$ -
177.77x3.90	1081	1.50	1.227	881	1180	1208	1.340	37.63	1.384	1.033
179.01x4.52	1266	1.75	1.229	1031	1427	1200	1.384	22.06	1.183	0.854
180.21x5.12	1450	2.00	1.230	1178	1477	1199	1.253	15.94	1.034	0.825
182.51x6.27	1811	2.50	1.233	1469	1746	1219	1.189	10.64	0.830	0.698
183.81x6.92	2022	2.79	1.235	1637	1885	1216	1.151	9.11	0.745	0.646

where

$$\alpha = 1 + \left( \frac{\pi^2 E_s}{2f_y} \cdot \frac{e_0}{L_{BRB}} \right) / \left( \frac{L_{BRB}}{D_e} \right) \quad (4)$$

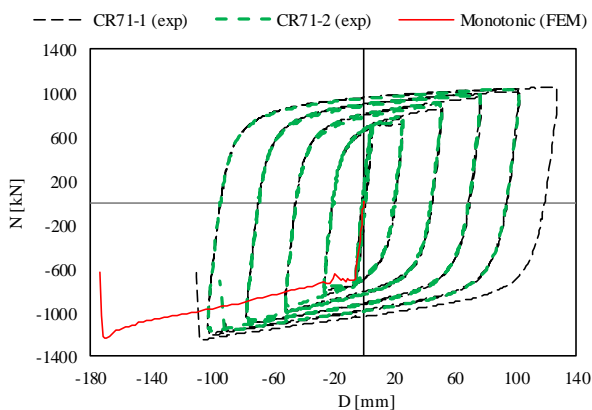


Fig. 14 Calibration of the equivalent imperfection of BRB model under monotonic compression loading

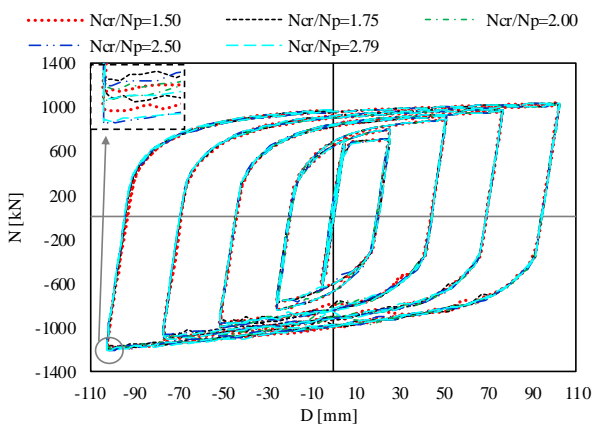


Fig. 15 Cyclic response of BRB models with BRMs of different strength

The analytical and the FEM results are summarized in Table 5. By analysing the ratio between the FEM and the analytical prediction of the design critical load ( $N_{Rd,f}/N_{Rd,a}$ ), it can be noticed that the formula is less conservative for stronger BRM. This happens due to the fact that the influence of the concrete infill, imperfection and other modelling assumptions to the buckling resistance of the FEM model becomes less important with larger thickness of the steel tube, thus the steel tube becomes the main component responsible for the strength of the buckling restraining mechanism.

In the second phase, cyclic analyses were performed on the BRB models with BRMs of different strength. As presented in Fig. 15, the cyclic response is stable for all models during the entire loading protocol ( $N_{Ed}/N_{Rd,f} \leq 1$ ). However, considering the maximum compression force  $C_{max} = 1219$  kN developed by the models under cyclic loading as the design force  $N_{Ed,BRM}$ , from Table 5 it can be observed that only the models with  $N_{cr}/N_p \geq 2.50$  are satisfying the design check  $N_{Ed,BRM}/N_{Rd,a} \leq 1.0$  proposed in Takeuchi and Wada (2017). It means that the analytical design approach is conservative. Nevertheless, the mid-span deflection ( $U_{y,mid}$ ) of the steel tube increases at a larger rate for small  $N_{cr}/N_p$  ratios. In the case of the model with  $N_{cr}/N_p = 1.50$ ,  $U_{y,mid}$  reached 37.63 mm, during the compression phase of the second cycle at  $2.0\Delta_{bm}$ . Moreover, the maximum compression force under cyclic loading for the model with  $N_{cr}/N_p = 1.5$  amounts to 1208 kN, which is larger than the resistance under monotonic loading,  $N_{Rd,f} = 1180$  kN. For larger  $N_{cr}/N_p$  values this "anomaly" is not observed.

As presented in section 2.6, the calibrated FEM model ( $N_{cr}/N_p = 1.53$ ) buckled during the first compression phase of the  $2.5\Delta_{bm}$  cycle under a force  $C_{max} = 1260$  kN, which is slightly larger than the maximum compression force recorded using the standard loading protocol from Fig. 13, with  $C_{max} = 1202$  kN.

Fig. 16 presents the state of stress in the steel tube at peak compression during the second cycle at  $2.0\Delta_{bm}$ . It can be observed that in the case of BRB model with  $N_{cr}/N_p = 1.50$  the maximum stress  $\sigma_{tube}^{max} = 462$  N/mm<sup>2</sup> is beyond the true yield strength of the tube,  $\sigma_{tube}^0 = 460$  N/mm<sup>2</sup>. For the other models, the maximum stress decreases as increasing the thickness of the tube.

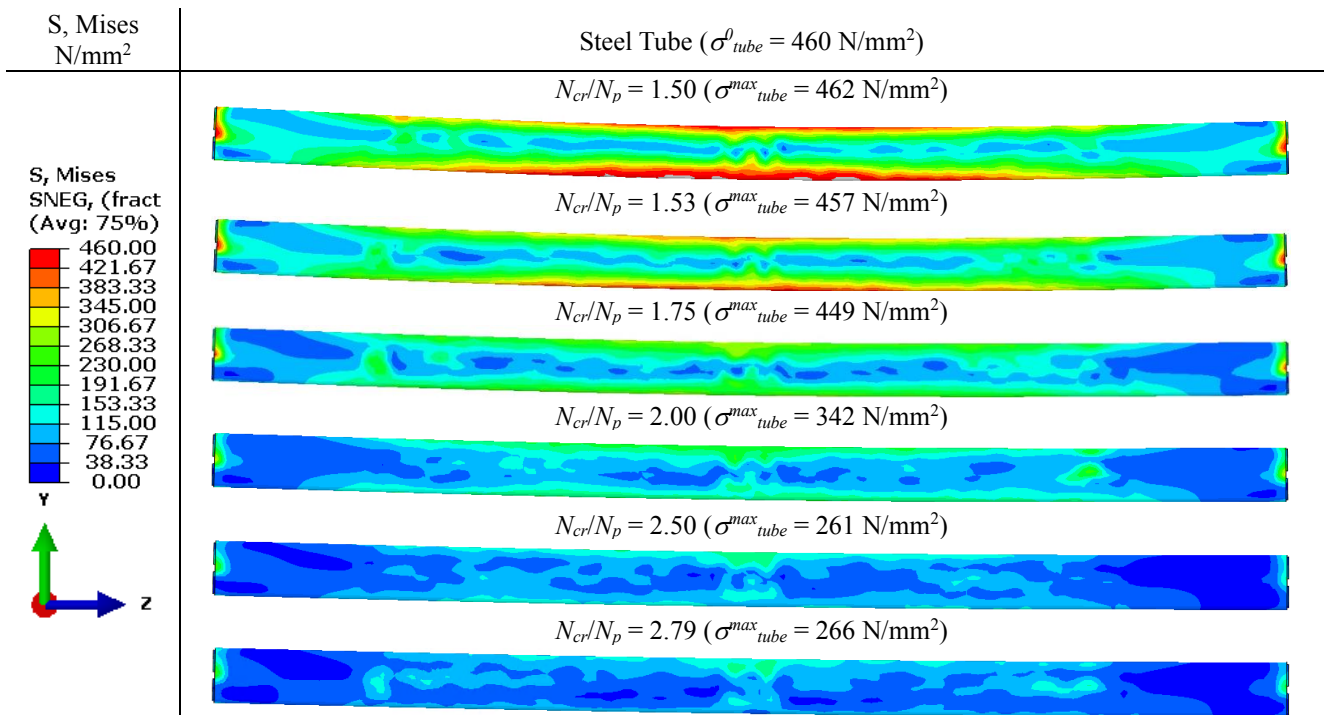


Fig. 16 State of stress in steel tube at peak compression during the second cycle at  $2.0D_{bm}$

Based on these facts, the model designed for  $N_{cr}/N_p = 1.50$  is considered sensitive to global buckling. This fact is also confirmed by analysing the  $N_{Ed, BRM} / N_{Rd, f}$  ratios from Table 5. In the case of BRB model with  $N_{cr}/N_p = 1.50$ , the ratio  $N_{Ed, BRM} / N_{Rd, f}$  is equal to 1.033, while for all the other models subunit ratios are obtained.

It can be concluded that the analytical procedure proposed by Watanabe *et al.* (1988), with a minimum ratio  $N_{cr}/N_p > 1.5$ , shows to be too simplistic and sometimes unconservative, since it does not take into account the maximum compression force,  $C_{max} = \beta \omega N_p$ , that could be developed by the BRB during cyclic loading. The analytical design procedure proposed by Takeuchi and Wada (2017) takes into account  $C_{max}$  and also second order effects ( $\alpha$ ). It is found that their design formula is more conservative than the one proposed by Watanabe *et al.* (1988), leading to  $N_{cr}/N_p$  ratios considerable larger than 1.5. Also, the design formula proposed by Takeuchi and Wada (2017) is less conservative for stronger buckling restraining mechanisms. To pass the design check  $N_{Ed, BRM} / N_{Rd, a} \leq 1.0$ , a minimum ratio  $N_{cr}/N_p > 2.5$  is needed to be used for the design of the BRM.

### 3.6 Concrete class

The influence of the class of concrete infill on the cyclic performance of BRB was investigated by assessing the response of four BRB models corresponding to CR73-2. The models are similar except for the concrete mechanical properties, which were modelled using the concrete damaged plasticity material (CDP), as described in section

3.4.2. In addition to the concrete class used for the calibrated BRB model, C30/37, the following concrete classes were chosen for this numerical study: low strength concrete C12/15, normal strength concrete C20/25, high strength concrete C50/60. The mechanical properties of the concrete material models used in these simulations are summarized in Table 6.

Table 6 Concrete material inputs

Class	$f_{cm}$ N/mm <sup>2</sup>	$f_{cm} / f_{cm(exp)}$	$E_{cm}$ N/mm <sup>2</sup>	$\nu$ -	$f_{ctm}$ N/mm <sup>2</sup>
C12/15	20	0.50	27088	0.2	1.6
C20/25	28	0.75	30303	0.2	2.2
C30/37 (exp.)	37.8	1.00	33503	0.2	2.9
C50/60	58	1.50	38629	0.2	4.1

Table 7 Performance parameters of BRB models with different concrete classes

Class	Concrete		Steel core		Tube	BRB
	PE	PEEQ	PE	PEEQ	$U_{y, mid}$ mm	$\beta$
C12/15	0.0309	0.0239	0.058	1.323	9.00	1.14
C20/25	0.0283	0.0177	0.063	1.449	8.64	1.13
C30/37	0.0169	0.0105	0.071	1.516	7.98	1.15
C50/60	0.0139	0.0085	0.071	1.487	8.27	1.16

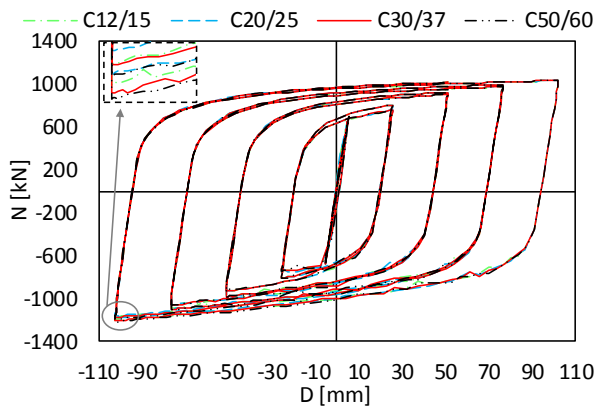


Fig. 17 Cyclic response of BRB models with the concrete infill of different classes

The axial force ( $N$ ) - displacement ( $D$ ) responses are presented in Fig. 17. It can be observed that there are no significant differences in the  $N$ - $D$  responses.

Table 7 presents the values of the plastic strain ( $PE$ ) and cumulative plastic strain ( $PEEQ$ ) in the concrete and the steel core obtained at the end of analysis. The table also gives the maximum values of the mid-span deflection of the steel tube ( $U_{y,mid}$ ) in the vertical plane  $YZ$ , see Fig. 23(a), and the compression strength adjustment factor ( $\beta$ ).

In the case of all BRB models the maximum value of plastic deformation occurred in the mid-zone of the concrete part, near the stopper. In the case of the BRB model C12/15, concentrations of plastic deformations occurred also at the top end of the concrete part, where the load is applied. Based on the results from Table 7 it can be noticed that the concrete part undergoes larger plastic and cumulative plastic strains if its class is lower (C12/15 and C20/25) in comparison to higher concrete classes (C30/37 and C50/60), with a level of magnitude of almost twice.

The mid-span deflection ( $U_{y,mid}$ ) of the steel tube has slightly larger values in the cases of lower concrete classes. On the other side, the  $PE$  and  $PEEQ$  values in the steel core are slightly increasing as the concrete class increases. This might be a consequence of increasing the elastic modulus of the concrete model, thus the concrete part is stiffer and less deformable, forcing the plastic deformations to develop in the core and not in the concrete part. The  $\beta$  factor is in the range of 1.13-1.16, with the lowest value recorded in the case of C20/25 ( $\beta=1.13$ ).

Based on the above numerical results, it can be concluded that the concrete class has little influence on the global performance of the BRB. However, in order to keep low levels of damage in concrete, it is prudent to use a concrete class of at least C30/37.

### 3.3 Steel properties

The dissipative component of a BRB is the steel core. Therefore, its properties are expected to have a major influence on the performance of the complete BRB. Four materials were considered such that to have a low (1.2) and

a high (1.6) value of the tensile to yield strength ratio ( $f_u/f_y$ ), and a small (0.22 mm/mm) and a larger (0.36 mm/mm) value of the rupture strain,  $\epsilon_r$ . All materials have the same yield stress ( $f_y = 394$  N/mm<sup>2</sup>), and the same strain at the onset of strain hardening,  $\epsilon_{sh}$  (0.015 mm/mm). The strain corresponding to the tensile strength,  $\epsilon_{tu}$ , was considered as 55 % of  $\epsilon_r$  based on experimental observations, while the rupture strength was considered as 80 % of  $f_u$ . The mechanical properties are summarized in Table.

Having the target properties set, the corresponding input material for Abaqus software was based on the calibration procedure described in Hu *et al.* (2016). Using the Abaqus/Explicit built-in combined isotropic-kinematic material model requires some modifications to the procedure for obtaining the material input data. The procedure uses tensile coupon test results to calibrate the input parameters which can be further used for either monotonic or cyclic FEM analyses.

The numerical stress-strain curves of the four materials under monotonic uniaxial tensile loading are presented in Fig. 18(a). They were obtained on numerical model of a standard specimen for tensile tests, with a proportional initial gauge length ( $L_0 = 5.65\sqrt{A_0}$ , where  $A_0$  is the initial cross-sectional area), discretized using C3D8I finite elements.

The cyclic stress-strain response of steel presented in Fig. 18(b) was obtained using a variable loading protocol with amplitudes that will generate similar strain levels as in the case of analyses on BRBs. A unit cube discretized with one finite element C3D8I was the numerical model for cyclic analyses since the strain range does not exceed  $\epsilon_u$  and therefore no necking is expected to occur.

Table 8 Mechanical properties of steel used for cores

Parameter	mat-1	mat-2	mat-3	mat-4
$f_y$ , N/mm <sup>2</sup>	394	394	394	394
$f_u$ , N/mm <sup>2</sup>	473	630	473	630
$f_r$ , N/mm <sup>2</sup>	378	504	378	504
$f_u/f_y$	1.20	1.60	1.20	1.60
$\epsilon_{sh}$ , -	0.015	0.015	0.015	0.015
$\epsilon_{tu}$ , -	0.121	0.121	0.198	0.198
$\epsilon_r$ , -	0.220	0.220	0.360	0.360
$\epsilon_u/\epsilon_r$	0.55	0.55	0.55	0.55

Table 9 Performance parameters of BRB models with different steel properties for the core

Material model	$\omega$ , -	$\beta$ , -	$\omega\beta$ , -	$CID/\Delta_{by}$	Cycles completed	$E_{dis}$ , kNm
mat-1	1.15	1.24	1.43	145	7	312
mat-2	1.49	1.25	1.86	265	9	688
mat-3	1.19	1.25	1.49	196	8	430
mat-4	1.54	1.28	1.98	334	10	845

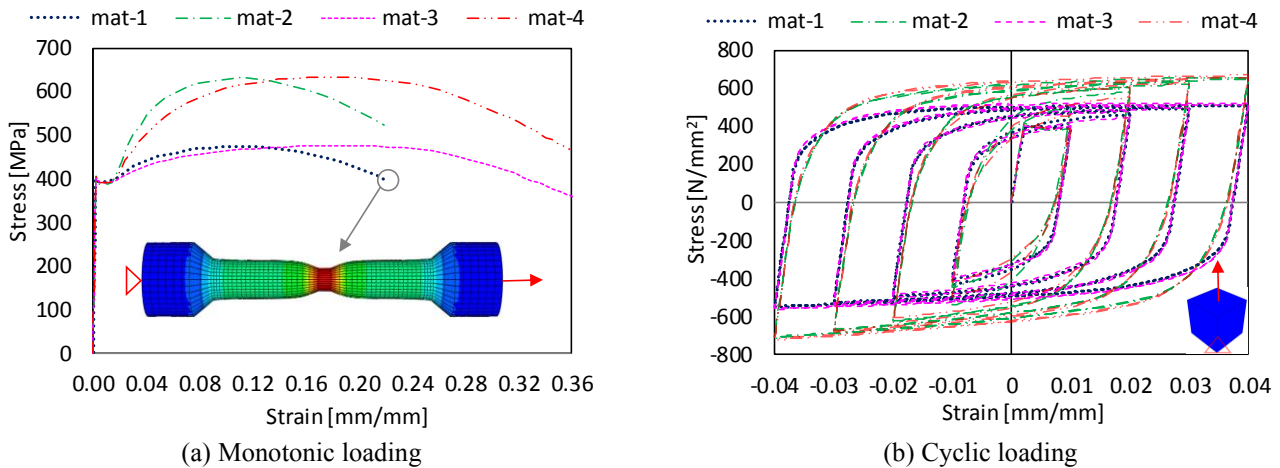


Fig. 18 Response of steel models under different loadings

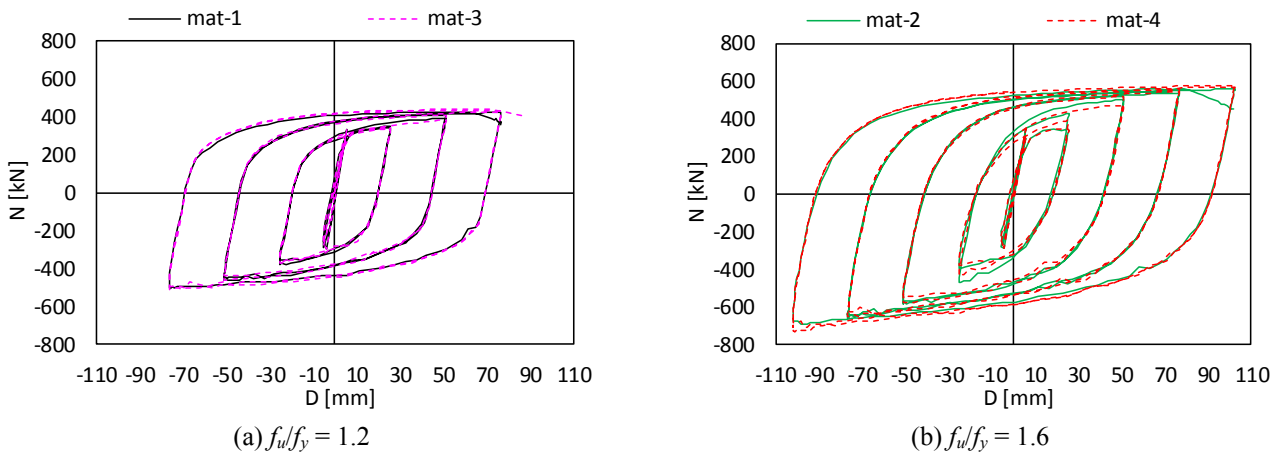


Fig.19 Influence of plastic properties of steel on BRB response under cyclic loading

The four materials were assigned to the core of the BRB model corresponding to CR33-1 specimen. Cyclic analyses were performed using the protocol from Fig. 13 and the axial force-displacement response of the four BRB models are presented in Figs. 19(a) and 19(b). It can be observed that only the BRB model having the material *mat-4* assigned to the core could sustain the entire loading protocol (10 cycles) without premature necking or fracture. The other models failed prematurely due to lack of ductility or low tensile to yield strength ratio.

The cyclic response of the BRB models is also evaluated with respect to the performance parameters presented in Table 9. As expected, the value of the strain hardening adjustment factor ( $\omega$ ) is larger in the cases of BRB models having  $f_u/f_y = 1.6$  (*mat-2* and *mat-4*), with a maximum value of  $\omega = 1.54$  for *mat-4* model. Also, the  $\omega\beta$  factor is higher for BRB models *mat-2* and *mat-4*. This increase leads to higher values of the maximum compression force which is used to design the non-dissipative components of the BRB (elastic segments of the core, BRM, connections). Consequently, larger sections might be needed.

On the other hand, the compression strength adjustment factor,  $\beta$ , (Table 9) is affected to a very low extent by the material properties (tensile to yield strength ratio and ultimate strain).

The cumulative inelastic deformation,  $CID$ , exceeded 200 times the yield deformation,  $\Delta_{by}$ , only in the case of the models with  $f_u/f_y = 1.6$  (*mat-2* and *mat-4*). Thus, the models *mat-1* and *mat-3* could not satisfy the ANSI/AISC 341-10 (2010) requirement for qualification.

With respect to the energy dissipated by the BRB,  $E_{dis}$ , computed as the area inside the hysteretic loops prior to necking, major differences can be observed between the BRB models. The larger value of  $E_{dis} = 845$  kNm was obtained in the case of BRB model *mat-4* which has the material defined by  $f_u/f_y = 1.6$  and  $\epsilon_r = 0.36$  mm/mm. Using a steel material of similar tensile to yield strength ratio ( $f_u/f_y = 1.6$ ) but less ductile ( $\epsilon_r = 0.22$  mm/mm) causes the dissipated energy to reduce with almost 19 % (case of BRB model *mat-2*). In the case of BRB models with  $f_u/f_y = 1.2$  (*mat-1* and *mat-3*), the dissipated energy is almost 50 % less in comparison to the models with  $f_u/f_y = 1.6$ .

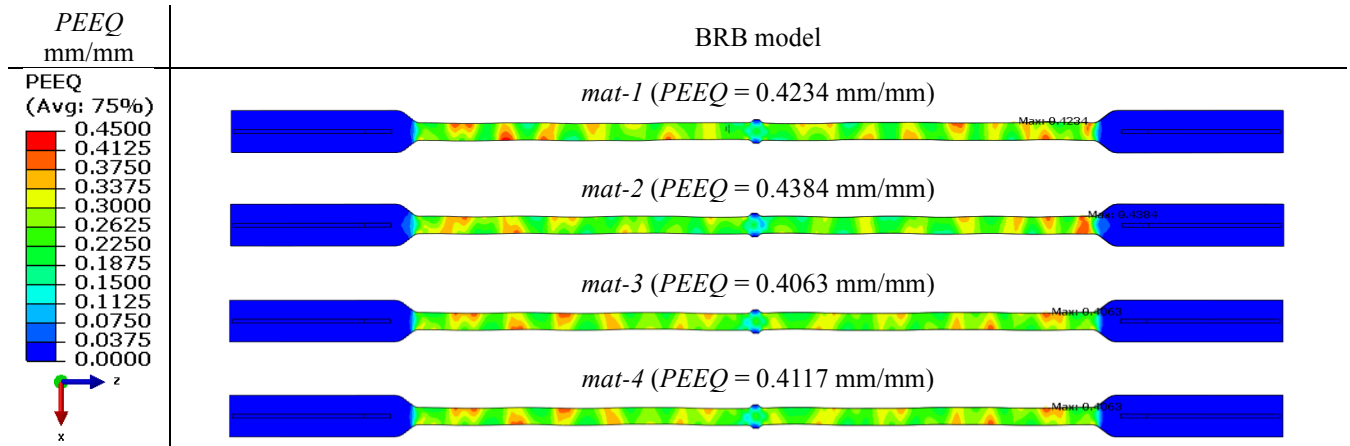


Fig. 20 State of cumulative plastic strain in core at peak compression during the first cycle at  $1.5D_{bm}$

It can be concluded that characteristics of the steel core are critical for the performance of BRBs. The tensile to yield strength ratio is by far the most important. Larger  $f_u/f_y$  values allow for redistribution of plastic strains over a longer portion of the core (Fig. 20), increasing the overall ductility of the BRB. They also lead to a significant improvement of energy-dissipation capacity. As a downside, larger  $f_u/f_y$  values of steel requires stronger non-dissipative components. Based on numerical simulations, but also on experimental results, values of  $f_u/f_y \geq 1.3$  and  $\varepsilon_r \geq 0.30$  are required to fulfil the qualification protocol from Fig. 13. It has to be reminded that the protocol is quite "severe", the design inter-storey drift  $\Delta_{bm}$  being equal to 2% of the storey height. Further studies are needed to generalise this conclusion for other BRB geometries, capacities, and loading protocols.

### 3.4 Self-weight loading

This numerical study aims at investigating the influence of self-weight load on the evolution of the plastic deformations in the plastic segments of the core. The top segment corresponds to the BRB end where the cyclic loading is applied, while the bottom segment to the fixed end.

For this investigation, four BRB models corresponding to specimens CR73-2 and CS73-2 were cyclically tested with and without self-weight load. The cyclic response of the tested BRBs expressed as reaction force ( $N$ ) and coreend displacement ( $D$ ), are presented in Fig. 21(a) for CR73-2 models and in Fig. 21(b) for CS73-2 models. No significant differences can be observed for the cases where the of self-weight load was included.

However, if analysing the time-history of the displacements between the tube and the top/bottom end of the core,  $D_{bt} / D_{bb}$ , in comparison to the core deformation,  $D_c$ , significant differences between the models can be observed. In the case of both CR73-2 and CS73-2 models, see Figs. 22 (a) and 22(c), the presence of self-weight load causes the top segment of the core to undergo larger deformations during the tensile loading in comparison to the

bottom segment, which undergoes larger deformations during the compressive loading. Therefore, the evolution of the plastic deformations in the plastic segments of the core under the presence of self-weight load is unsymmetrical.

In the case of the BRB models where the self-weight load was not included, see Figs. 22(b) and 22(d), the evolution of the plastic deformations in the plastic segments of the core is more uniform in comparison to the models with self-weight load. In the case of CR73-2 model, the asymmetry is still more pronounced with respect to CS73-2.

To quantify this effect, maximum deformation ratios in the top ( $R_t$ ) and bottom ( $R_b$ ) parts of the core were determined for the  $2.0\Delta_{bm}$  cycles

$$R_t = D_{bt}/D_c \quad (2)$$

$$R_b = D_{bb}/D_c \quad (6)$$

Maximum deformation ratios  $R_t$  and  $R_b$  are summarized in Table 10. Ideally, for a symmetrical response, both rations would be equal to 0.5. For all except one model (CR73-2-noG), the deformation ratios in the top segment of the core are larger in tension ( $R_t = 0.52-0.64$ ), while in the bottom part of the core the deformation ratios are larger in compression ( $R_b = 0.52-0.63$ ).

In the case of CR73-2 models (with self-weight, CR73-2-G, and without self-weight, CR73-2-noG) the asymmetry is more pronounced in comparison to CS73 models, with deformation ratios varying between  $R_t = 0.44-0.64$  and  $R_b = 0.37-0.63$ .

Table 10 Maximum deformation ratios  $R_t$  and  $R_b$

BRB model	$R_t$		$R_b$	
	Tens.	Compr.	Tens.	Compr.
CR73-2-G	0.64	0.44	0.37	0.63
CR73-2-noG	0.44	0.56	0.56	0.45
CS73-2-G	0.59	0.47	0.45	0.55
CS73-2-noG	0.52	0.51	0.51	0.52

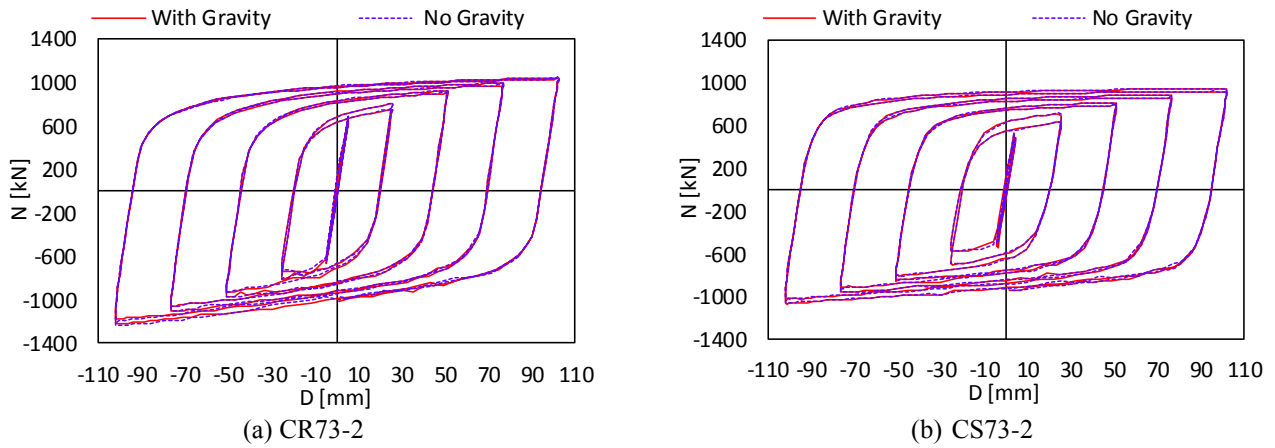


Fig. 21 Influence of self-weight loading on the cyclic response of BRB models

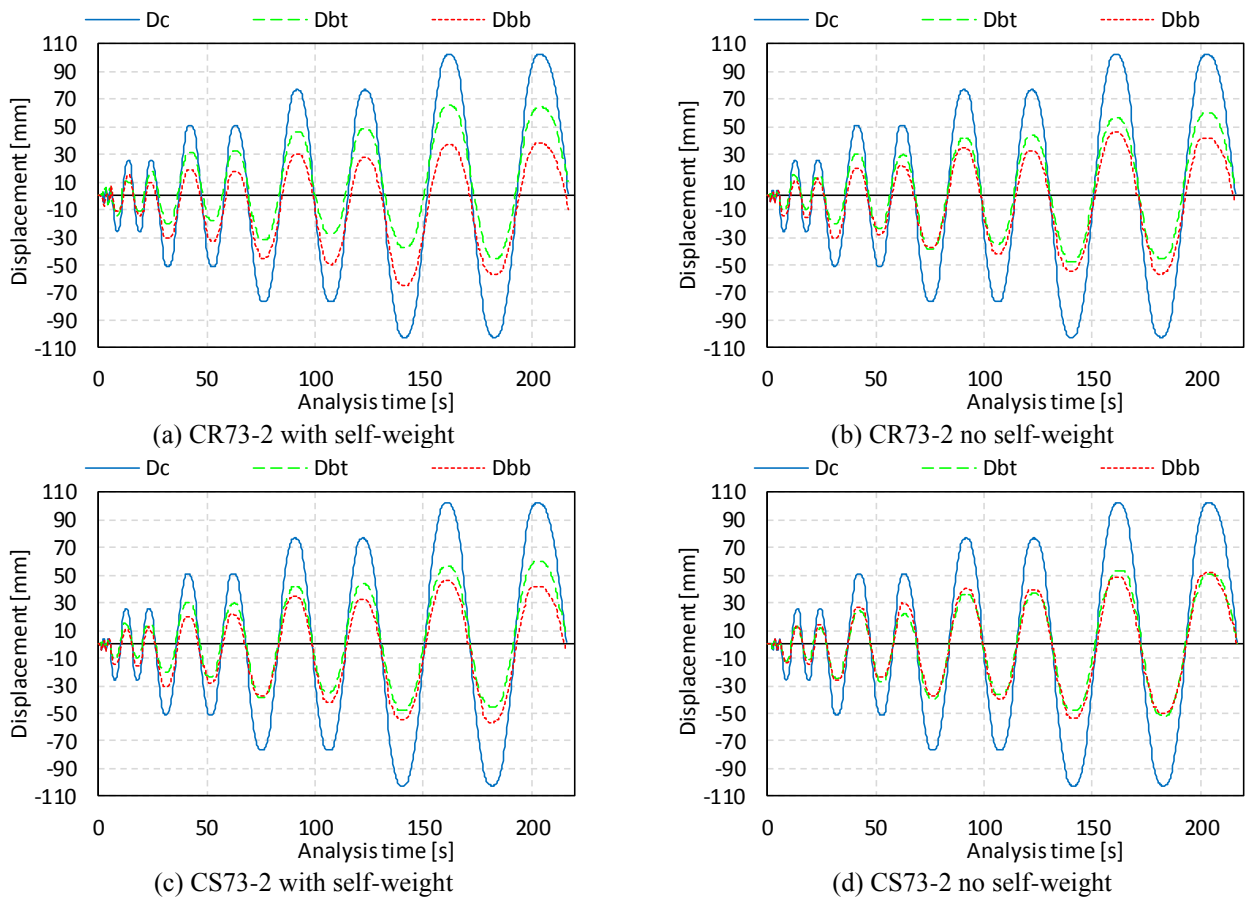


Fig. 22 FEM relative displacements: tube-to-core ( $D_{bt}$ ,  $D_{bb}$ ) vs. core end-to-end ( $D_c$ )

In the case of CS73-2 models (CS73-2-G and CS73-2-noG), a more uniform distribution of plastic deformations is obtained, with deformation ratios varying between  $R_t = 0.47-0.59$  and  $R_b = 0.45-0.55$ .

The absence of self-weight load causes the deformation ratios  $R_t$  and  $R_b$  to approach to 0.5.

### 3.5 Frame effect

The influence of the frame effect, in addition to the uniaxial cyclic loading (see section 2.2), on the BRB cyclic performance was investigated on two models corresponding to specimen CR71-1. The models are similar, except for the loading scheme, see Fig. 23(a). In the case of the first model

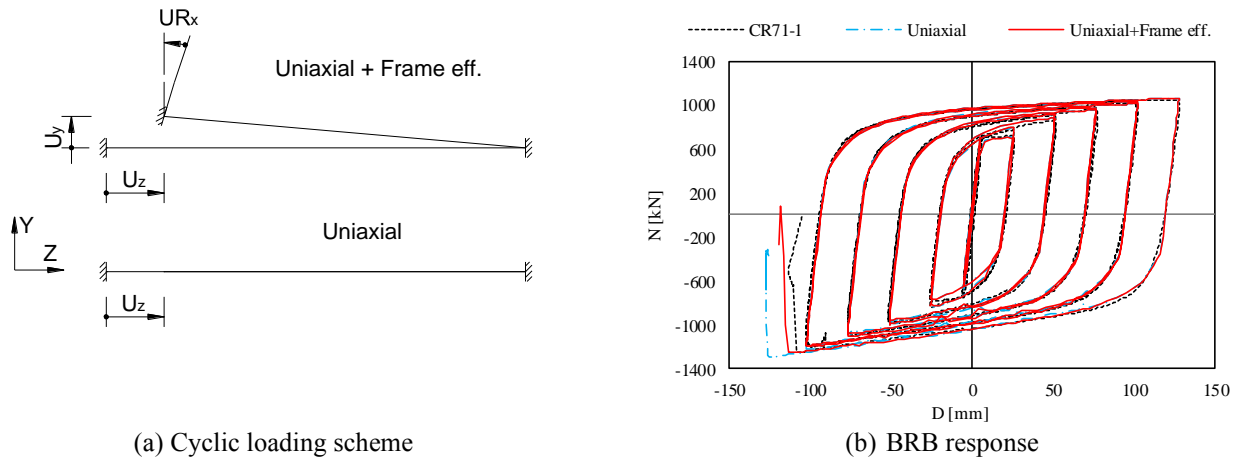


Fig. 23 Influence of the loading scheme on the response of the BRB model

(Uniaxial), only the axial load  $U_z$  was applied. For the second model (Uniaxial + Frame eff.) axial  $U_z$ , transversal  $U_y$ , and rotational  $UR_x$  loads were applied. Based on the results presented in Fig. 23(b), it can be observed that the additional frame effect leads to slightly lower resistance to overall buckling. In comparison to the maximum compression force experimentally recorded for CR71-1,  $C_{max} = 1258$  kN, a closer prediction is obtained in the case of modelling both uniaxial and the frame effect,  $C_{max} = 1260$  kN, while in the case of the uniaxially loaded model the maximum compression force is slightly larger,  $C_{max} = 1296$  kN.

Accounting for the frame effect in addition to axial BRB loading leads to slightly better prediction of the experimental response in case when global buckling occurs. However, for the analysed connection detail, frame effect has little influence on the BRB response when it behaves as intended (no overall buckling).

#### 4. Conclusions

A complex nonlinear numerical model of the buckling restrained brace was developed in the finite element environment Abaqus. The calibration against experimental data was performed at both component level (material models: steel, concrete, unbonding material) and BRB level (loading, geometrical initial imperfections). Geometrically and materially nonlinear analyses including imperfections (GMNIA) were performed on BRB models under cyclic loading. Close predictions were obtained for all FEM models. The calibrated models were further used to perform a parametric study aiming at understanding some phenomena related to BRB cyclic behaviour. Five main aspects were numerically investigated by running cyclic analyses and assessing the performance of the BRB models: the strength of the buckling restraining mechanism, concrete class of the infill material, mechanical properties of steel used for the core, self-weight loading and frame effect.

The design procedure of the buckling restraining mechanism was validated based on FEM results. The analytical procedure proposed by Watanabe *et al.* (1988), with a minimum ratio of the critical elastic force of the BRM to the plastic resistance of the core,  $N_{cr}/N_p > 1.5$ , showed to be too simplistic and sometimes unconservative. It was found that the analytical design procedure proposed by Takeuchi and Wada (2017) is more appropriate.

Concrete class of the infill has little influence on the global performance of the BRB. However, to keep low levels of damage in concrete, it is prudent to use a concrete class of at least C30/37.

Characteristics of the steel core are critical for the performance of BRBs. Based on numerical simulations, but also on experimental results, values of  $f_u/f_y \geq 1.3$  and  $\varepsilon_r \geq 0.30$  are required to fulfil the qualification protocol. Further studies are needed to generalise this conclusion for other BRB geometries, capacities, and loading protocols.

The presence of self-weight loading leads to unsymmetrical evolution of deformations in the plastic segments of the core. This phenomenon is more pronounced in the case of BRB model of type A (core with a rectangular cross-section) in comparison to BRB model of type B (core with square cross-section).

If BRB-column sub-assembly setup is used for experimental tests, when performing FEM analyses the cyclic loading applied to the BRB model should consider both uniaxial and frame effect loading to achieve close predictions.

#### Acknowledgements

The research leading to these results has received funding from the MEN-UEFISCDI grant Partnerships in priority areas PN II, contract no. 99/2014 IMSER: "Implementation into Romanian seismic resistant design practice of buckling restrained braces". This support is gratefully acknowledged.

## References

- AlHamaydeh, M., Abed, F. and Mustapha, A. (2016), “Key parameters influencing performance and failure modes for BRBs”, *J. Constr. Steel Res.*, **116**, 1-18. <https://doi.org/10.1016/j.jcsr.2015.08.038>.
- ANSI/AISC 341-10 (2010), Seismic Provisions for Structural Steel Buildings, American Institute of Steel Construction, Chicago, IL, USA.
- Budaházy, V. and Dunai, L. (2015), “Numerical analysis of concrete filled Buckling Restrained Braces”, *J. Constr. Steel Res.*, **115**, 92-105. <https://doi.org/10.1016/j.jcsr.2015.07.028>.
- Chou, C.C. and Chen, S.Y. (2010), “Subassembly tests and finite element analyses of sandwiched buckling-restrained braces”, *Eng. Struct.*, **32**(8), 2108-2121. <https://doi.org/10.1016/j.engstruct.2010.03.014>.
- Chen, Q., Wang, C.L., Meng, S. and Zeng, B. (2016), “Effect of the unbonding materials on the mechanic behavior of all-steel buckling-restrained braces”, *Eng. Struct.*, **111**, 478-493. <https://doi.org/10.1016/j.engstruct.2015.12.030>.
- D’Aniello, M., Della Corte, G. and Landolfo, R. (2014), “Finite element modelling and analysis of “all-steel” dismantlable buckling restrained braces”, *The Open Construction and Building Technology Journal*, **8** (Suppl 1: M4), 216-226.
- Dassault (2014), Abaqus 6.14 - Abaqus Analysis User’s Manual, Dassault Systèmes Simulia Corp.
- Dehghani, M. and Tremblay, R. (2017), “An analytical model for estimating restrainer design forces in bolted buckling restrained braces”, *J. Constr. Steel Res.*, **138**, 608-620. <https://doi.org/10.1016/j.jcsr.2017.07.007>.
- Dusika, P. and Tinker, J. (2013), “Global Restraint in Ultra-Lightweight Buckling-Restrained Braces”, *J. Compos. Constr.*, **17**, 139-150. [https://doi.org/10.1061/\(ASCE\)CC.1943-5614.0000320](https://doi.org/10.1061/(ASCE)CC.1943-5614.0000320).
- EN 1992-1-1 (2004), Eurocode 2: Design of concrete structures – Part 1-1: General rules and rules for buildings, European Committee for Standardization; Brussels, Belgium.
- EN 1993-1-1 (2005), Eurocode 3: Design of steel structures – Part 1-1: General rules and rules for buildings, European Committee for Standardization; Brussels, Belgium.
- Eryasar, E. (2009), “Experimental and numerical investigation of buckling restrained braces”, Master Thesis, Middle East Technical University, Ankara, Turkey.
- Genna, F. and Gelfi, P. (2012), “Analysis of the lateral thrust in bolted steel buckling-restrained braces. I: experimental and numerical results”, *J. Struct. Eng.*, **138**(10), 1231-1243. [https://doi.org/10.1061/\(ASCE\)ST.1943-541X.0000558](https://doi.org/10.1061/(ASCE)ST.1943-541X.0000558).
- Ghowsi, A.F. and Sahoo, D.R. (2019), “Effect of loading history and restraining parameters on cyclic response of steel BRBs”, *Int. J. Steel Struct.*, **19**(4), 1055-1069. <https://doi.org/10.1007/s13296-018-0187-7>.
- Ghowsi, A.F. and Sahoo, D.R. (2015), “Fragility assessment of buckling-restrained braced frames under near-field earthquakes”, *Steel Compos. Struct.*, **19**(1), 173-190. <https://doi.org/10.12989/scs.2015.19.1.173>.
- Guo, Y.L., Tong, J.Z., Wang, X.A. and Zhang, B.H. (2017), “Subassembly tests and numerical analyses of buckling-restrained braces under pre-compression”, *Eng. Struct.*, **138**, 473-489. <https://doi.org/10.1016/j.engstruct.2017.02.046>.
- Hadianfard, M.A., Eskandari, F. and JavidSharifi, B. (2018), “The effects of beam-column connections on behavior of buckling-restrained braced frames”, *Steel Compos. Struct.*, **28**(3), 309-318. <https://doi.org/10.12989/scs.2018.28.3.309>.
- Hoveidae, N. and Rafezy, B. (2012), “Overall buckling behavior of all-steel buckling restrained braces”, *J. Constr. Steel Res.*, **79**, 151-158. <https://doi.org/10.1016/j.jcsr.2012.07.022>.
- Hu F., Shi G. and Shi, Y. (2016), “Constitutive model for full-range elasto-plastic behavior of structural steels with yield plateau: Calibration and validation”, *Eng. Struct.*, **118**, 210-227. <https://doi.org/10.1016/j.engstruct.2016.03.060>.
- Inoue, K., Sawaizumi S., Higashibata, Y. and Inoue, K. (1992), “Buckling stiffening design of reinforced concrete wall panel with built-in unbonded flat steel bar braces”, *J. Struct. Constr. Eng.*, **432**, 41-49.
- Iwata, M. and Murai, M. (2006), “Buckling-restrained brace using steel mortar planks; performance evaluation as a hysteretic damper”, *Earthq. Eng. Struct. D.*, **35**, 1807-1826. <https://doi.org/10.1002/eqe.608>.
- Lemaitre, J. and Chaboche, J.L. (1990), *Mechanics of Solid Materials*, Cambridge University Press, Cambridge, U.K.
- Korzekwa, A. and Tremblay, R. (2009), *Numerical Simulation of the Cyclic Inelastic Behaviour of Buckling Restrained Braces*, Taylor & Francis Group, London, UK, 653-658.
- Matsui, R., Takeuchi, T., Hajjar, J.F., Nishimoto, K., and Aiken, I. (2008), “Local buckling restraint condition for core plates in buckling-restrained braces”, *Proceedings of the 14th World Conf. on Earthquake Eng.*, Beijing, China, October.
- Montazerian, L. and Mohammadreza, N.S. (2015), “Finite element simulation of the energy dissipation capacities for buckling restrained braces”, *Can. J. Basic Appl. Sci.*, **3**(11), 290-295.
- Mostafa, A.A. (2013), “Nonlinear finite element modeling of the load-carrying and energy dissipation capacities for buckling-restrained braces”, Master dissertation, Faculty of the American University of Sharjah, College of Engineering, Sharjah, United Arab Emirates.
- Pandikkadavath, M.S. and Sahoo, D.R. (2016), “Analytical investigation on cyclic response of buckling-restrained braces with short yielding core segments”, *Int. J. Steel Struct.*, **16**(4), 1273-1285. <https://doi.org/10.1007/s13296-016-0083-y>.
- Park, J., Lee, J. and Kim, J. (2012), “Cyclic test of buckling restrained braces composed of square steel rods and steel tube”, *Steel Compos. Struct.*, **13**(5), 423-436. <https://doi.org/10.12989/scs.2012.13.5.423>.
- Piedrafitra, D., Maimi, P. and Cahis, X. (2015), “A constitutive model for a novel modular all-steel buckling restrained brace”, *Eng. Struct.*, **100**, 326-331.
- Rahai, A. and Mortazavi, M. (2014), “Experimental and numerical study on the effect of core shape and concrete cover length on the behavior of BRBs”, *Int. J. Civil Eng.*, **12**(4), 379-395.
- Rahai, A., Alinia, M. and Salehi, S. (2009), “Cyclic performance of buckling restrained composite braces composed of selected materials”, *Int. J. Civil Eng.*, **1**(7), 1-8.
- Razavi, S.A., Mirghaderi, S.R., seini, A. and Shemshadian, M.E. (2012), “Reduced length buckling restrained brace using steel plates as restraining segment”, *Proceedings of the 15th World Conference on Earthquake Eng.*, Lisbon, Portugal, September.
- Razavi Tabatabaei, S.A., Mirghaderi, S.R. and Hosseini, A. (2014), “Experimental and numerical developing of reduced length buckling-restrained braces”, *Eng. Struct.*, **77**, 143-160.
- Razavi, S.A., Kianmehr, A., Hosseini, A. and Mirghaderi, S.R. (2018), “Buckling-restrained brace with CFRP encasing: Mechanical behavior & cyclic response”, *Steel Compos. Struct.*, **27**(6), 675-689. <https://doi.org/10.12989/scs.2018.27.6.675>.
- Saeki, E., Iwamatu, K. and Wada, A. (1996a), “Analytical study by finite element method and comparison with experiment results concerning buckling-restrained unbonded braces”, *J. Struct. Constr. Eng.*, **484**, 111-120.
- Saeki, E., Maeda, Y., Iwamatsu, K. and Wada, A. (1996b), “Analytical study on unbonded braces fixed in a frame”, *J. Struct. Constr. Eng.*, **489**, 95-104.
- Stratan, A., Zub, C.I. and Dubina, D. (in press), “Prequalification of a set of buckling restrained braces: Part I – experimental tests”, *Steel and Composite Structures*, (in print).
- Talebi, E., Tahir, M., Zahmatkesh, F., Yasreen, A. and Mirza, J.

- (2014), "Thermal behavior of cylindrical buckling restrained braces at elevated temperatures", *Sci. World J.*, **2014**, 1-13.
- Talebi, E., Tahir, M., Zahmatkesh, F. and Kueh, A. (2015), "A numerical analysis on the performance of buckling restrained braces at fire-study of the gap filler effect", *Steel Compos. Struct.*, **19**(3), 661-678.  
<https://doi.org/10.12989/scs.2015.19.3.661>.
- Takeuchi, T. and Wada, A. (2017), *Buckling-Restrained Braces and Applications*, The Japan Society of Seismic Isolation (JSSI), Jingumae Shibuyaku Tokyo, Japan.
- Tinker, J.A. (2011), "Development of an Ultra-Lightweight Buckling Restrained Brace Using Analytical and Numerical Methods", Master dissertation, Portland State Univ., OR, USA.
- Korzekwa, A. and Tremblay, R. (2009), *Numerical Simulation of the Cyclic Inelastic Behaviour of Buckling Restrained Braces*, Taylor & Francis Group, London, UK, 653-658.
- Watanabe, A., Hitomi, Y., Saeki, E., Wada, A. and Fujimoto, M. (1988), "Properties of brace encased in buckling restraining concrete and steel tube", *Proceedings of the 9th World Conf. Earthquake Engineering*, Tokyo, Japan, August.
- Wu, A.C., Lin, P.C. and Tsai, K.C. (2014), "High-mode buckling responses of buckling-restrained brace core plates", *Earthq. Eng. Struct. D.*, **43**(3), 375-393.  
<https://doi.org/10.1002/eqe.2349>.
- Xie, Q., Zhou, Z., Huang, J.H., Zhu, D.P. and Meng, S.P. (2016), "Finite-element analysis of dual-tube self-centering buckling-restrained braces with composite tendons", *J. Compos. Constr.*, **21**(3), 04016112. [https://doi.org/10.1061/\(ASCE\)CC.1943-5614.0000778](https://doi.org/10.1061/(ASCE)CC.1943-5614.0000778).
- Yazdi, H.M., Mosalman, M. and Soltani, A.M. (2018), "Seismic study of buckling restrained", *Int. J. Steel Struct.*, **18**(1), 153-162.
- Zub, C.I., Stratan, A., Dogariu, A. and Dubina, D. (2018), "Development of a finite element model for a buckling restrained brace", *Proceedings of the Romanian Academy Series A*, **19**(4), 581-588.